TDP-43 pathology disrupts nuclear pore complexes and nucleocytoplasmic transport in ALS/FTD

Ching-Chieh Chou[1,2,15], Yi Zhang [1,3,16], Mfon E. Umoh[2,4], Spencer W. Vaughan [5], Ileana Lorenzini[6], Feilin Liu[7,8], Melissa Sayegh[5], Paul G. Donlin-Asp[1,17], Yu Han Chen[1], Duc M. Duong[2,9], Nicholas T. Seyfried[2,4,9], Maureen A. Powers[1], Thomas Kukar[2,4,10], Chadwick M. Hales[2,4], Marla Gearing[2,4,11], Nigel J. Cairns[12], Kevin B. Boylan[13], Dennis W. Dickson [7], Rosa Rademakers[7], Yong-Jie Zhang[7], Leonard Petrucelli[7], Rita Sattler[6], Daniela C. Zarnescu[5], Jonathan D. Glass[2,4,14] and Wilfried Rossoll [1,2,7]*

The cytoplasmic mislocalization and aggregation of TAR DNA-binding protein-43 (TDP-43) is a common histopathological hallmark of the amyotrophic lateral sclerosis and frontotemporal dementia disease spectrum (ALS/FTD). However, the composition of aggregates and their contribution to the disease process remain unknown. Here we used proximity-dependent biotin identification (BioID) to interrogate the interactome of detergent-insoluble TDP-43 aggregates and found them enriched for components of the nuclear pore complex and nucleocytoplasmic transport machinery. Aggregated and disease-linked mutant TDP-43 triggered the sequestration and/or mislocalization of nucleoporins and transport factors, and interfered with nuclear protein import and RNA export in mouse primary cortical neurons, human fibroblasts and induced pluripotent stem cell–derived neurons. Nuclear pore pathology is present in brain tissue in cases of sporadic ALS and those involving genetic mutations in *TARDBP* and *C9orf72*. Our data strongly implicate TDP-43-mediated nucleocytoplasmic transport defects as a common disease mechanism in ALS/FTD.

ALS and FTD are relentlessly progressive and fatal neurodegenerative disorders that show a considerable overlap in genetics, clinical features and neuropathology, suggesting that they are part of a disease spectrum[1]. A common histopathological hallmark in ALS/FTD patient brains is the cytoplasmic mislocalization of the predominately nuclear RNA-binding TDP-43 and the accumulation of its hyperphosphorylated and ubiquitinated C-terminal fragment (CTF) in detergent-insoluble aggregates[2,3]. This pathology is observed in ~97% of ALS and ~50% of FTD cases, but also frequently present in other neurodegenerative diseases[1]. TDP-43 is encoded by the *TARDBP* gene and contains two RNA-recognition motifs, a nuclear localization sequence (NLS) and a nuclear export signal (NES), allowing it to shuttle between the nucleus and cytosol. The C-terminal glycine-rich region consists of a low-complexity domain with a prion-like Gln/Asn-rich sequence, which mediates protein–protein interactions[4]. Remarkably, the C terminus harbors most of the disease-causing missense mutations identified in ALS/FTD patients, which promote cytoplasmic

mislocalization and neurotoxicity of TDP-43[5–7]. Under environmental stress conditions, persistent stress granule formation in the cytosol may increase stability of TDP-43 and facilitate aggregation[8]. Although aberrant sequestration of RNA-binding proteins and other interacting proteins could lead to impaired RNA and protein homeostasis[1], the exact molecular mechanism by which TDP-43 pathology (that is, cytoplasmic aggregation or mutation of TDP-43) causes neurodegeneration remains poorly understood.

To explore the mechanisms through which TDP-43 pathology contributes to neurodegeneration, we adapted the BioID method to interrogate the proteome of detergent-insoluble cytoplasmic TDP-43 aggregates. Our proteomic analysis identified components of nucleocytoplasmic transport pathways as a major group of proteins present in the pathological TDP-43 aggregates. Morphological and functional analyses in primary cortical neurons, patient fibroblasts and stem cell–derived neurons confirmed that TDP-43 pathology causes the mislocalization and/or aggregation of nucleoporins (Nups) and transport factors (TFs), as well as disruption of nuclear
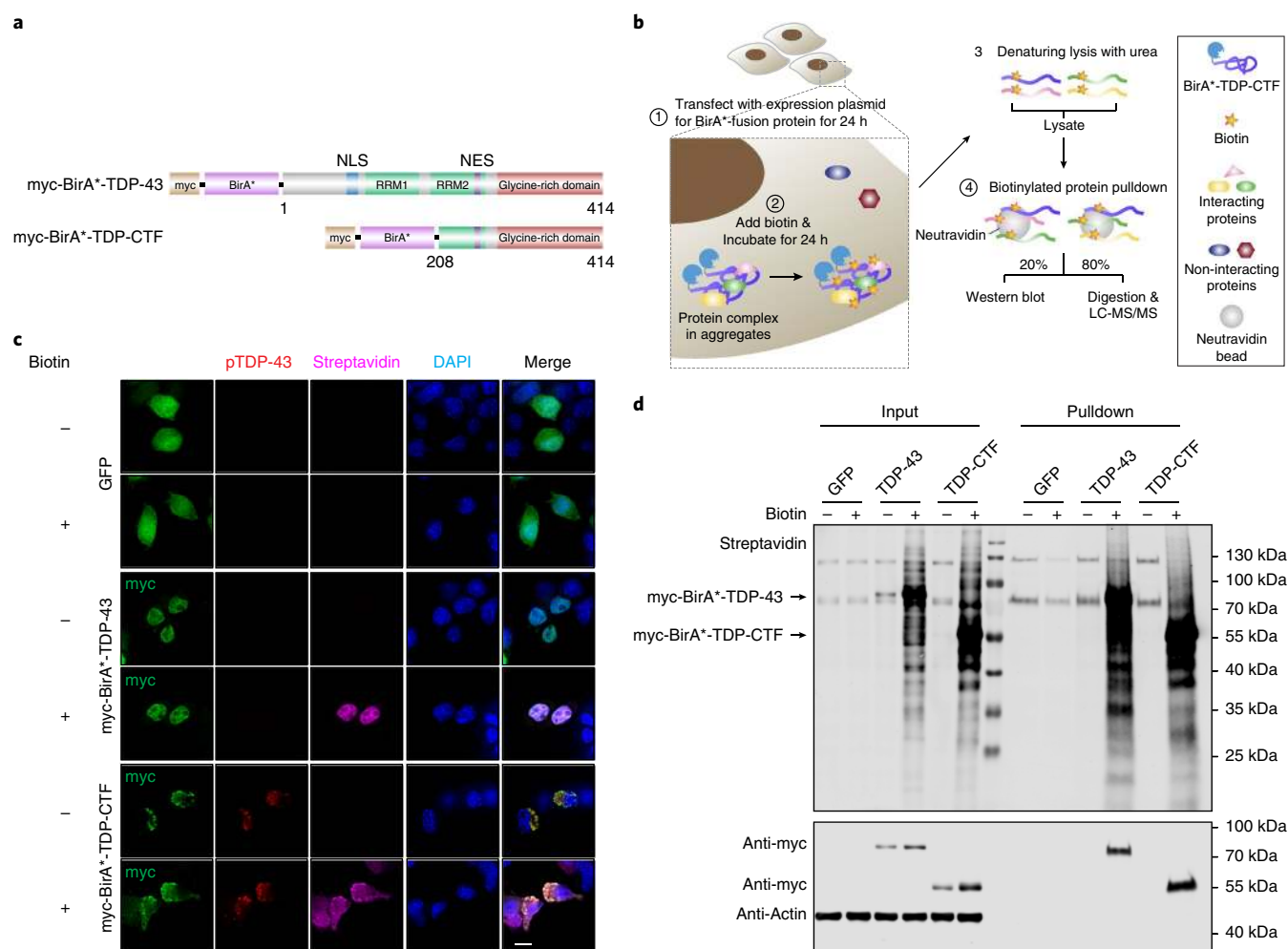
Fig. 1 | A modified BioID method identifies the composition of pathological detergent-insoluble TDP-43 aggregates. a, Domain structures of myc-BirA* fusion constructs with human full-length TDP-43 and TDP-CTF protein. **b**, Schematic for the proximity-dependent biotinylation and identification of proteins associated with myc-BirA*-TDP-CTF. **c**, Anti-myc staining shows nuclear myc-BirA*-TDP-43 and cytoplasmic aggregates of myc-BirA*-TDP-CTF (green) that are positive for pTDP-43 (Ser409/Ser410) (red) and biotin (magenta). **d**, Western blot analysis of biotinylated proteins in lysates and after pulldown with neutravidin beads. These experiments were repeated three times with similar results. Uncropped blots are provided in Supplementary Fig. 17. Scale bar: 10 μm.

membrane (NM) and nuclear pore complexes (NPCs), leading to reduced nuclear protein import and mRNA export. In addition, mutations in *Nup* genes acted as genetic modifiers in *Drosophila melanogaster* models of TDP-43 proteinopathy. Our findings of Nup205 pathology in brain tissue from sporadic ALS (sALS) and *TARDBP* mutation-associated ALS (TDP-ALS) point to nucleo-cytoplasmic transport defects caused by TDP-43 pathology as a common disease mechanism in ALS/FTD, and potentially other TDP-43 proteinopathies.

Results

Cytoplasmic TDP-43 aggregates are enriched for components of nucleocytoplasmic transport pathways. A 25-kDa C-terminal fragment of TDP-43 (TDP-CTF) generated by proteolytic cleavage at Arg208 is found as a major component of insoluble cytoplasmic aggregates in ALS/FTD patients' brain tissue[3]. Its expression as a fusion protein in vitro recapitulates histopathological features present in human patients[9–11]. To characterize changes in the interaction partners of TDP-43 under normal and pathological conditions, we used the BioID approach, which is based on the fusion of a promiscuous mutant of *Escherichia coli* biotin ligase (BirA*) to proteins of interest and catalyzes the biotinylation of proximate proteins in the natural cellular environment[12,13].

To determine physiological and aggregate-specific interacting partners of TDP-43, we transfected Neuro-2A (N2a) neuroblastoma cells with expression vectors for myc-BirA*-tagged human TDP-43 (myc-BirA*-TDP-43) or TDP-CTF (myc-BirA*-TDP-CTF) (Fig. 1a). Cells were incubated with excess biotin in the culture media to induce biotinylation of proximate proteins (Supplementary Fig. 1a,b), followed by denaturing lysis in 8 M urea, to solubilize protein aggregates, and affinity purification via neutravidin beads (Fig. 1b). Biotinylated proteins colocalized with myc-BirA*-TDP-43 in the nucleus and with myc-BirA*-TDP-CTF in cytoplasmic aggregates that were positive for hyperphosphorylated TDP-43 (pTDP-43 Ser409/Ser410), ubiquitin and p62/SQSTM1 (Fig. 1c and Supplementary Fig. 1c,d). Proximity-dependent biotinylation of myc-BirA*-TDP-43- and myc-BirA*-TDP-CTF-associated proteins showed distinct patterns in western blots (Fig. 1d).

Affinity-purified biotinylated proteins were subjected to unbiased proteomic analysis. We found 254 proteins associated with myc-BirA*-TDP-43 and 389 proteins associated with myc-BirA*-TDP-CTF (Fig. 2a). Clustering analysis of the TDP-43- or TDP-CTF-associated proteome versus a mock-transfected control based on gene ontology (GO) in DAVID identified distinct categories of strongest interacting proteins. The top categories in the TDP-43/Mock comparison were mRNA processing and splicing, whereas
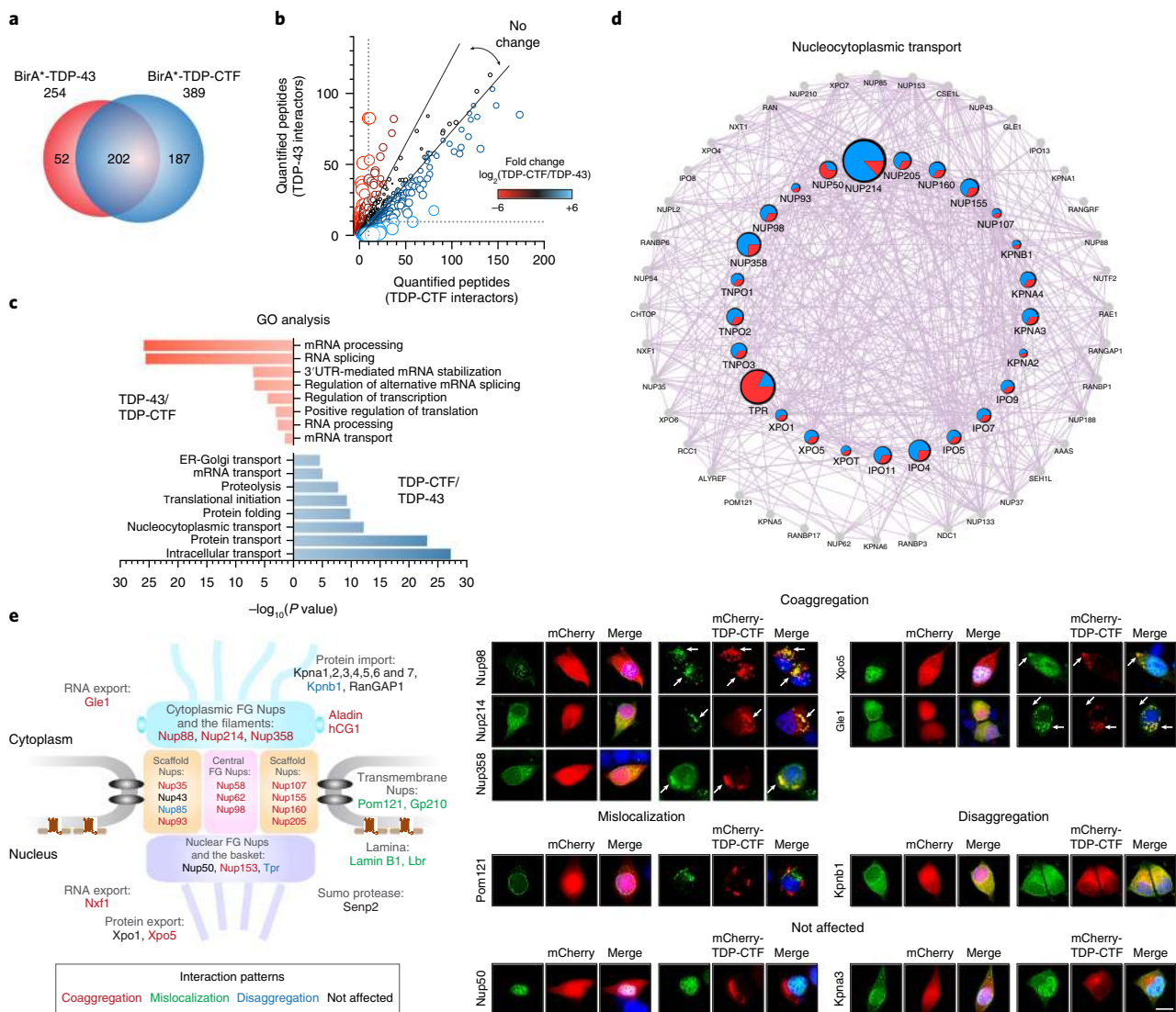
Fig. 2 | Pathological TDP-43 aggregates contain components of the nucleocytoplasmic transport machinery. a, Mass spectrometry analysis of proximity-biotinylated proteins associated with BirA*-TDP-43 and BirA*-TDP-CTF. The 202 proteins present in both datasets accounted for 80% of the TDP-43- and 52% of the TDP-CTF-associated proteome. **b**, Mapping the number of identified peptide spectra matches for the interacting protein of TDP-43 and TDP-CTF (circle). The relative abundance ratio ($\log_2$-fold change) between TDP-CTF- and TDP-43-associated proteome is shown by circle size and color. Positive values indicate predominant association with TDP-CTF (blue), negative values with TDP-43 (red). The dotted line indicates the cut-off threshold. **c**, Gene ontology (GO) analysis of proteins preferentially associated with TDP-43 or TDP-CTF. P values indicate the probability of seeing that number of proteins annotated to a particular GO term, given the proportion of proteins in the total mouse proteome that are annotated to that GO term. **d**, Network analysis of the TDP-CTF versus TDP-43 proteome in the nucleocytoplasmic transport pathway by GeneMANIA. Gray circles represent unidentified proteins. Colored circles represent the identified proteins and their peptide spectra matches in the TDP-CTF- and TDP-43-associated proteomes (blue and red, respectively). Circle sizes reflect $\log_2$-fold change between TDP-CTF and TDP-43. **e**, Summary diagram of the TDP-CTF interaction screen with 37 proteins involved in nucleocytoplasmic transport (left) and representative images of the coaggregation (arrows) of GFP-tagged proteins with mCherry-TDP-CTF in N2a cells (right). Images for all tested components of the nucleocytoplasmic transport machinery are shown in Supplementary Figs. 4 and 5. Each experiment was repeated independently two to four times. Scale bar: 10 μm.

those in the TDP-CTF/Mock comparison were intracellular protein transport and translation initiation (Supplementary Fig. 2a,b). We further characterized the differences in the function-specific enrichment and interaction networks by comparing the TDP-CTF- and TDP-43-associated proteomes (Fig. 2b,c). Proteins involved in mRNA processing primarily associated with TDP-43 (Supplementary Fig. 2c), whereas the TDP-CTF associated proteome was enriched for proteins involved in intracellular transport (Supplementary Fig. 2d). Our network analysis also showed comparable results in biological processes (Supplementary Fig. 3). Notably, we identified components of nucleocytoplasmic transport

pathway as a major subset of protein interactors within TDP-CTF aggregates (Fig. 2d).

TDP-43 pathology causes the cytoplasmic aggregation and mislocalization of Nups and TFs. NPCs are multiprotein channels that act as gatekeepers regulating the receptor-mediated nucleocytoplasmic transport of macromolecules. NPCs contain ~30 different Nups and are among the largest proteinaceous assemblies in the eukaryotic cell[14]. To confirm putative TDP-CTF-associated proteins detected in our proteomic screen, we coexpressed Nups or TFs together with TDP-CTF in N2a cells. We identified four different
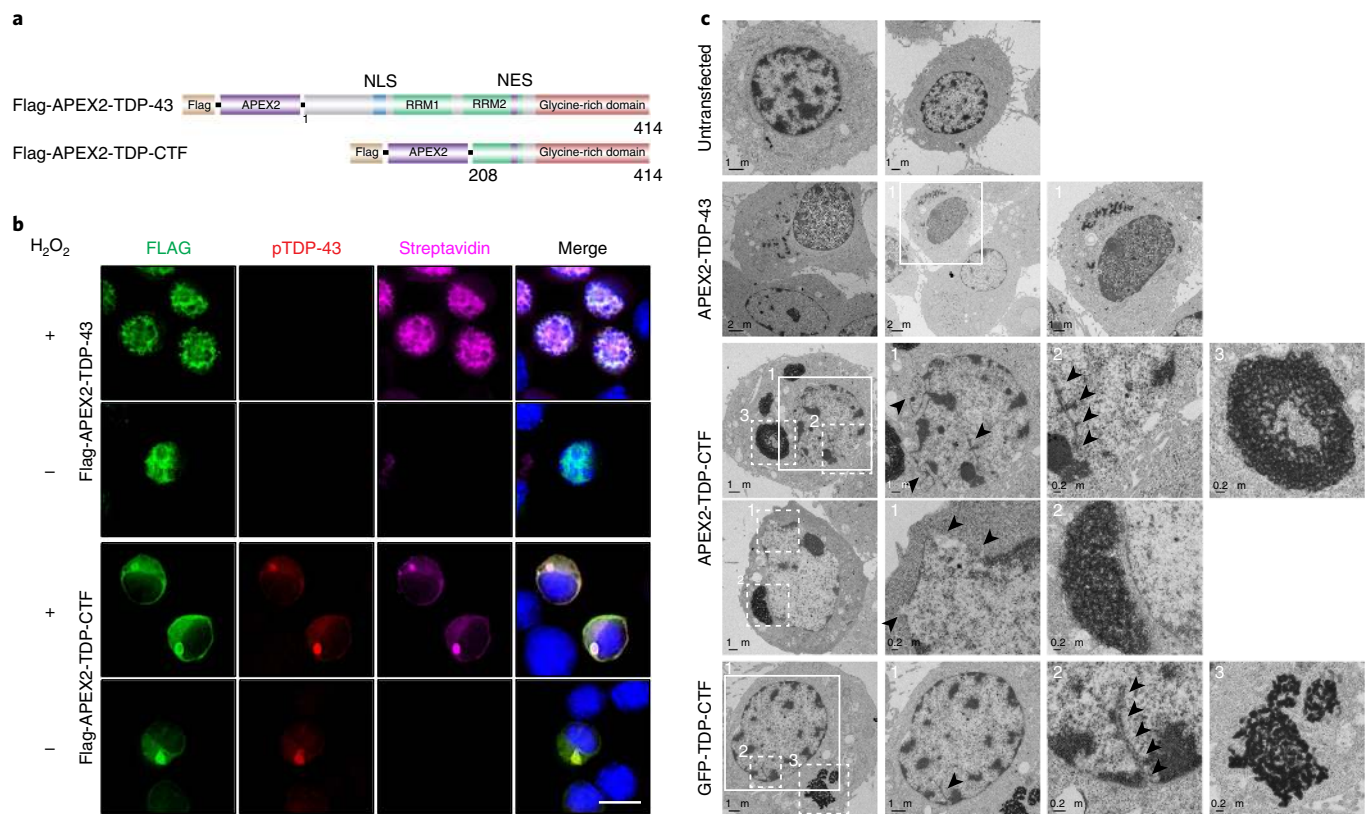
Fig. 3 | Electron microscopy analysis reveals abnormal NM morphology in N2a cells containing TDP-CTF aggregates. a, Schematic domain structures of engineered peroxidase, APEX2, fusion TDP-43 and TDP-CTF. **b**, Nuclear signals of Flag-APEX2-TDP-43 and cytoplasmic aggregates of Flag-APEX2-TDP-CTF were detected by anti-Flag antibody (green). TDP-CTF phosphorylation was detected by anti-pTDP-43 (Ser409/Ser410) antibody (red). Protein biotinylation catalyzed by APEX2 was detected by Cy5-conjugated streptavidin (magenta). Scale bar: 10 μm. **c**, Electron microscopy of untransfected N2a cells and cells expressing Flag-APEX2-TDP-43, Flag-APEX2-TDP-CTF or GFP-TDP-CTF. Untransfected cells showed dense chromatin and round nuclei. APEX2 catalyzed the deposition of diaminobenzidine (DAB) near nuclear APEX2-TDP-43 and in cytoplasmic APEX2-TDP-CTF aggregates. APEX2-TDP-CTF- as well as GFP-TDP-CTF-expressing cells exhibited irregularly shaped nuclei with deep invaginations of the NM. Each experiment was repeated independently three times with similar results.

interaction patterns, as summarized in the schematic of the NPC (Fig. 2e and Supplementary Figs. 4 and 5): (1) coaggregation with TDP-CTF was predominantly found for phenylalanine-glycine (FG) repeat-containing Nups, scaffold Nups and nuclear export factors; (2) mislocalization but no coaggregation was found in transmembrane Nups and nuclear lamina proteins, indicating a major structural disruption of the NPCs; (3) Nup85, Tpr and Kpnb1 caused disaggregation of TDP-CTF; and (4) there was no or only a minor effect on the nuclear FG-Nups as well as nuclear import factors. A list of coaggregation scores is presented in Supplementary Table 1.

ALS-linked missense mutations, such as Q331K and M337V, increase cytoplasmic TDP-43 mislocalization and neurotoxicity[15]. To test whether wild-type TDP-43 (TDP-43^{WT}) or mutant TDP-43 affect the localization of Nups and TFs, we expressed Nups or TFs together with TDP-43^{WT} or TDP-43^{Q331K} in N2a cells. Both TDP-43^{WT} and TDP-43^{Q331K} triggered the cytoplasmic aggregation of Nup62, whereas TDP-43^{Q331K} increased the propensity for cytoplasmic mislocalization of Nup98 and cytoplasmic aggregation of Nup93, Nup107 and Nup214 (Supplementary Fig. 6). Our results show that TDP-CTF alters the cellular localization of nucleocytoplasmic transport proteins to varying degrees. Although mutant TDP-43 does not induce visible aggregates in this cell culture model, it can still compromise the localization of a subset of FG-Nups.

FG-Nups contain prion-like domains (PrLDs) that mediate the cytoplasmic coaggregation with TDP-CTF. TDP-43 harbors a

low-complexity domain and PrLD at the C terminus, which contributes to self-assembly and protein–protein interactions[8]. PrLDs are frequently found in transcription factors and RNA-binding proteins[16], but have been recently identified in the FG-rich domains of yeast Nups[17]. FG repeats are also present in mammalian Nups and form amyloid-like interactions within sieve-like hydrogels and natively unfolded sites that act as effective barriers to normal macromolecules, but are permeable to shuttling nuclear transport receptor complexes[18].

We used the PLAAC algorithm and other online tools (see Methods) to identify prion-like and low-complexity sequences in human Nups and TFs. Quantitative analysis revealed the presence of a PrLD and low-complexity domain in the hydrogel-forming Nup214[19] and other FG-Nups including Nup54, Nup98, Nup153 and Nup358, but not Nup50 (Supplementary Fig. 7). To investigate whether PrLDs can mediate the coaggregation with TDP-CTF, we generated and coexpressed the PrLD or non-PrLD fragment of Nup98, Nup153 and Nup214. We found that PrLDs of Nup98 and Nup214 were both required and sufficient to mediate cytoplasmic coaggregation (Supplementary Fig. 8). Notably, although Nup153 PrLD had a weak coaggregation tendency with TDP-CTF, it caused dramatic mislocalization of both exogenous and endogenous full-length TDP-43.

TDP-43 pathology disrupts the morphology of the NM and NPCs. To visualize the nuclear morphology of transfected cells
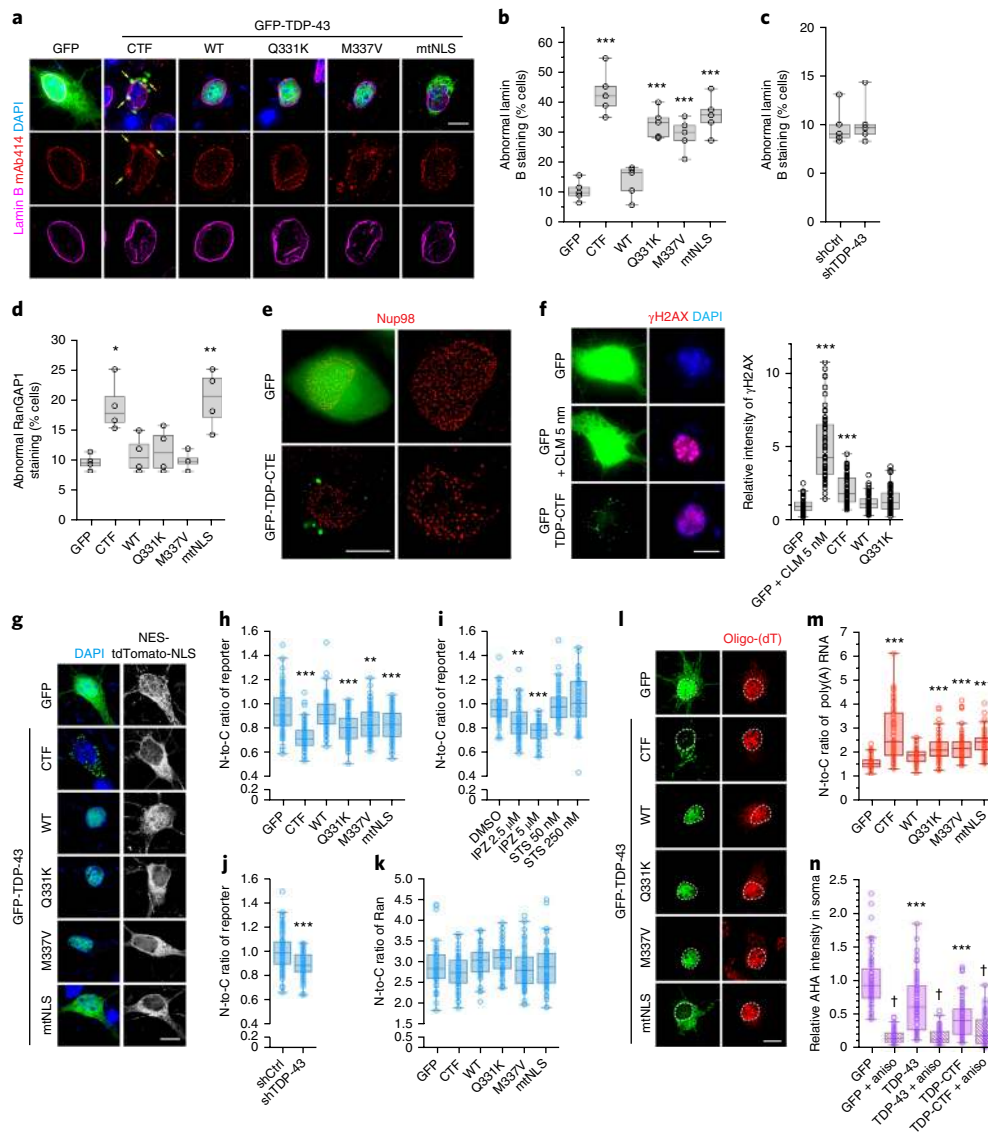
Fig. 4 | TDP-43 pathology disrupts NPC and nuclear lamina morphology and nucleocytoplasmic transport. a, Immunofluorescence (IF) of endogenous FG-Nups (mAb414, red) and lamin B (magenta) in primary cortical neurons expressing GFP or GFP-tagged TDP-CTF, TDP-43^{WT}, TDP-43^{Q331K}, TDP-43^{M337V} or TDP-43^{mtNLS}. This experiment was repeated independently five times. Arrows indicate colocalization of TDP-CTF and endogenous FG-Nups; scale bar, 10 μm. **b,c**, The percentage of transfected cells exhibiting abnormal lamin B staining (invagination, distortion) after transfection with TDP-43 expression vectors (**b**) or TDP-43 knockdown constructs (**c**). **d**, The percentage of transfected cells exhibiting abnormal RanGAP1 staining. **e**, Super-resolution IF imaging of endogenous Nup98 (red) in N2a cells expressing GFP or GFP-TDP-CTF. Scale bar: 10 μm. **f**, IF and quantification of mean γH2AX intensity in cortical neurons expressing GFP or GFP-tagged TDP-CTF, TDP-43^{WT} or TDP-43^{Q331K}. Calicheamicin (CLM) was added at 5 nM to induce DNA damage. **g–i**, IF and quantification of N-to-C ratio of a transport reporter encoding NES-tdTomato-NLS in cortical neurons expressing GFP or GFP-tagged TDP-43 constructs (**g,h**) or with treatment of staurosporine (STS) or importazole (IPZ) Scale bar: 10 μm. **i**. This experiment was repeated independently three times. **j**, Quantification of N-to-C ratio of reporter in neurons with TDP-43 knockdown. **k**, Quantification of the N-to-C ratio of Ran in neurons expressing GFP or GFP-tagged TDP-43 constructs. **l,m**, IF and quantification of N-to-C ratio of poly(A) RNA. Poly(A) RNA was detected by fluorescence in situ hybridization (FISH) with oligo(dT) probes (red). **l**, Quantification of newly synthesized protein via metabolic labeling with azidohomoalanine (AHA). Anisomycin (aniso) was added as a translation inhibitor. Scale bar: 10 μm. Graphs represent quartiles (boxes), 50th percentiles (center lines) and range (whiskers). Five independent experiments for **b** (circles represent each independent experiment; ***$P < 0.001$, one-way ANOVA), five independent experiments for **c** (circles represent each independent experiment; two-sided unpaired t-test), four independent experiments for **d** (circles represent each independent experiment; *$P < 0.05$, **$P < 0.01$, one-way ANOVA), three independent experiments for **f** (circles represent, for GFP: $n = 58$, GFP + CLM 5 nM: $n = 59$, TDP-CTF: $n = 61$, TDP-43^{WT}: $n = 59$ and TDP-43^{Q331K}: $n = 57$; ***$P < 0.001$, one-way ANOVA), three independent experiments for **h** (circles represent, for GFP: $n = 70$, TDP-CTF: $n = 72$, TDP-43^{WT}: $n = 70$, TDP-43^{Q331K}: $n = 70$, TDP-43^{M337V}: $n = 70$, TDP-43^{mtNLS}: $n = 61$; **$P < 0.01$, ***$P < 0.001$, one-way ANOVA), three independent experiments for **i** (circles represent, for DMSO: $n = 46$, IPZ 2.5 μM: $n = 45$, IPZ 5 μM: $n = 45$, STS 50 nM: $n = 46$, STS 250 nM: $n = 47$; **$P < 0.01$, ***$P < 0.001$, one-way ANOVA), four independent experiments for **j** (circles represent, for nonsilencing control shRNA (shCtrl): $n = 77$, TDP-43 shRNA (shTDP-43): $n = 80$; ***$P < 0.001$, two-sided unpaired t-test), three independent experiments for **k** (circles represent, for GFP: $n = 43$, TDP-CTF: $n = 44$, TDP-43^{WT}: $n = 36$, TDP-43^{Q331K}: $n = 51$, TDP-43^{M337V}: $n = 46$, TDP-43^{mtNLS}: $n = 48$; one-way ANOVA), three independent experiments for **m** (circles represent, for GFP: $n = 46$, TDP-CTF: $n = 61$, TDP-43^{WT}: $n = 49$, TDP-43^{Q331K}: $n = 51$, TDP-43^{M337V}: $n = 60$, TDP-43^{mtNLS}: $n = 58$; ***$P < 0.001$, one-way ANOVA), five independent experiments for **n** (circles represent, for GFP: $n = 58$, TDP-43^{WT}: $n = 58$, TDP-CTF: $n = 63$, GFP + aniso: $n = 59$, TDP-43^{WT} + aniso: $n = 55$, TDP-CTF + aniso: $n = 53$; ***$P < 0.001$, †$P < 0.001$, two-way ANOVA). Bonferroni's post hoc test. Full statistical details are provided in Supplementary Table 4. Scale bars in **a**, **e** and **g**: 10 μm.
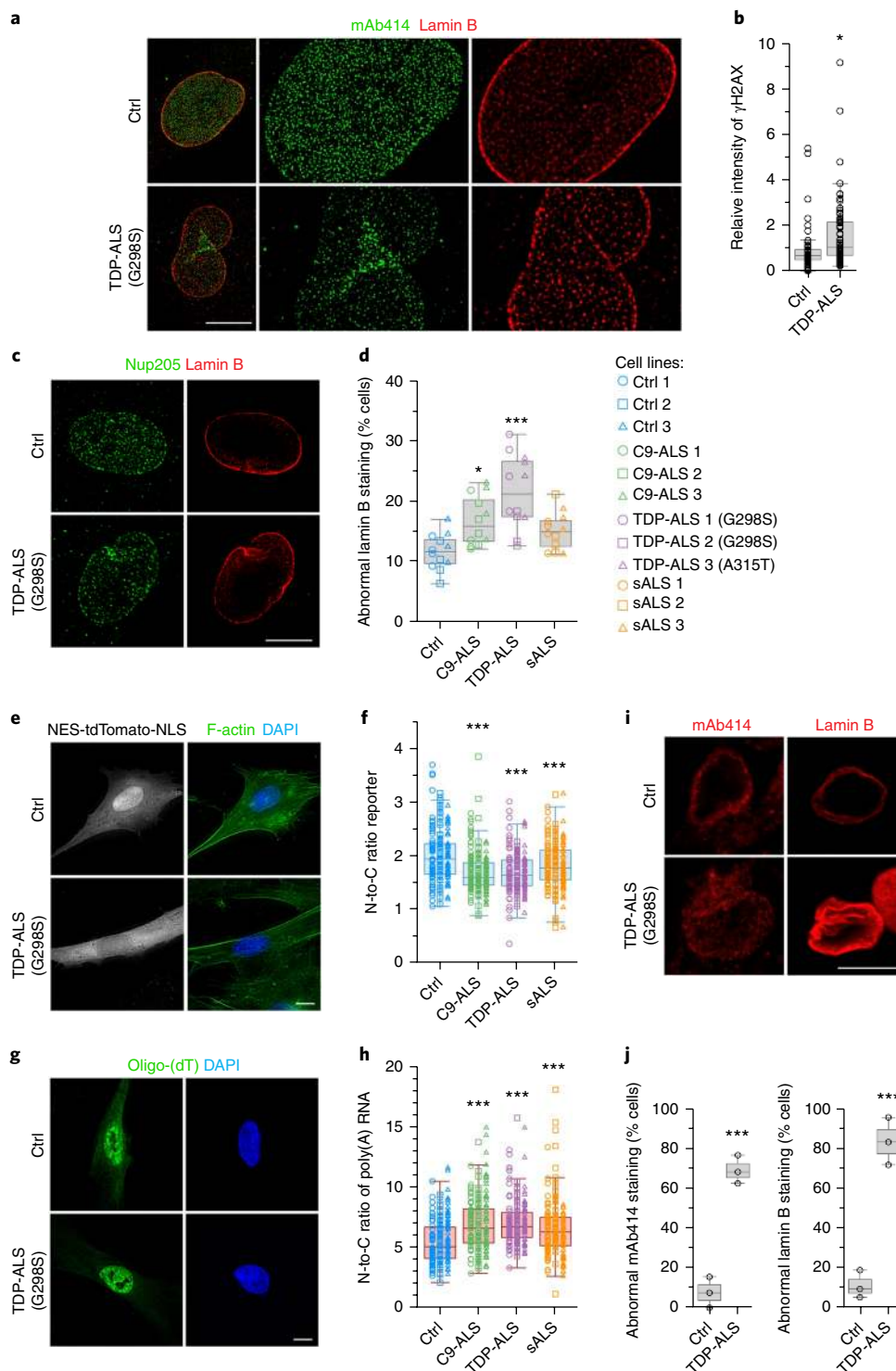
Fig. 5 | Human cells from ALS patients exhibit defects in NPC and nuclear lamina morphology and nucleocytoplasmic transport. a, Super-resolution immunofluorescence (IF) imaging of endogenous FG-Nups (mAb414, green) and lamin B (red) in fibroblasts from healthy control (Ctrl) and TDP-ALS. This was repeated independently three times with similar results. Scale bar: 10 μm. **b**, IF and quantification of mean anti-γH2AX intensity. **c,d**, IF of endogenous Nup205 (green) and lamin B (red; **c**) and quantification of cells with abnormal lamin B staining in fibroblasts from three control (Ctrl), C9-ALS, TDP-ALS and sALS cases (**d**). **e,f**, IF and quantification of N-to-C ratio of a transport reporter. **g,h**, IF and quantification of N-to-C ratio of poly(A) RNA. **i,j**, IF and quantification of cells with abnormal FG-Nups and lamin B staining in iPSC-derived motor neurons from Ctrl and TDP-ALS. Scale bar: 10 μm. Graphs represent quartiles (boxes), 50th percentiles (center lines) and range (whiskers). Five independent experiments for **b** (circles represent, for Ctrl: $n = 51$, TDP-ALS: $n = 62$; *$P < 0.05$, two-sided unpaired t-test), four independent experiments for **d** (symbols represent each independent experiment per cell line; *$P < 0.05$, ***$P < 0.001$, one-way ANOVA), four independent experiments for **f** (symbols represent, for Ctrl: $n = 178$, C9-ALS: $n = 175$, TDP-ALS: $n = 183$, sALS: $n = 180$; ***$P < 0.001$, one-way ANOVA), four independent experiments for **h** (symbols represent, for Ctrl: $n = 186$, C9-ALS: $n = 180$, TDP-ALS: $n = 190$, sALS: $n = 181$; ***$P < 0.001$, one-way ANOVA) and triplicates for each group for **j** (symbols represent each independent experiment; ***$P < 0.001$, two-sided unpaired t-test). Bonferroni's post hoc test. Full statistical details are provided in Supplementary Table 4. Scale bars in **c**, **e** and **g**: 10 μm.
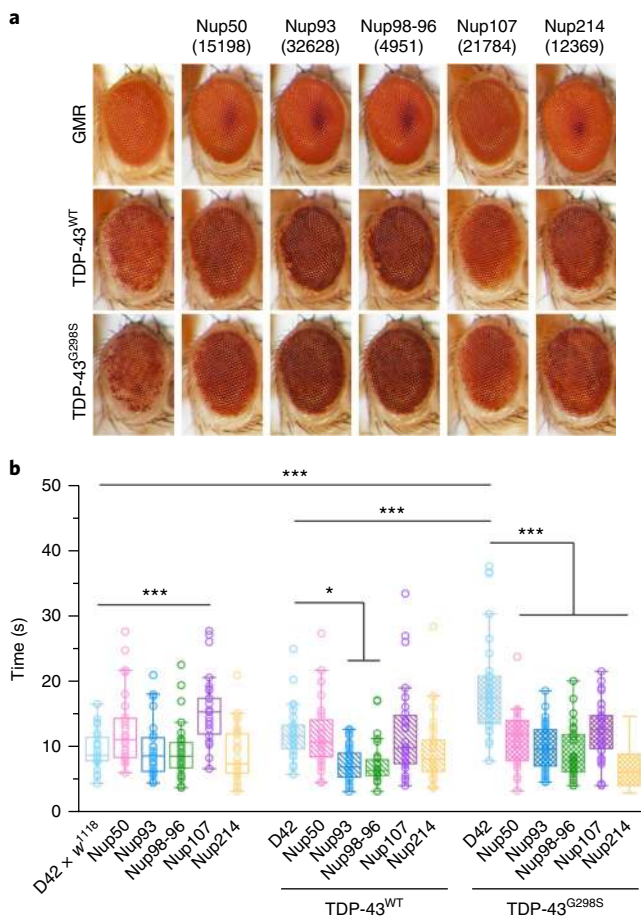
Fig. 6 | Identification of genetic suppression of TDP-43 toxicity in *Drosophila* disease models of ALS. a,b, Overexpression of human TDP-43[WT] and TDP-43[G298S] in *Drosophila* leads to neurodegeneration in the adult retina (**a**) and impairment in larval locomotor function (**b**). GMR GAL4 and D42 GAL4 driver lines were used for expression in the retina and motor neurons, respectively. *w[1118]* was used as a control fly line. Loss-of-function mutations in several *Drosophila* Nup genes rescue the phenotypes caused by TDP-43 pathology. Graph represents quartiles (boxes), 50th percentiles (center lines) and range (whiskers) in **b** (dots represent, for D42 × *w[1118]*: *n* = 26, others: *n* = 30 animals; *$P < 0.05$, ***$P < 0.001$, two-way ANOVA), Bonferroni's post hoc test. Full statistical details are provided in Supplementary Table 4.

at high resolution in electron microscopy, we fused TDP-43 and TDP-CTF to the engineered peroxidase APEX2, which functions as an electron microscopy tag[20] (Fig. 3a). APEX2-TDP-CTF formed pTDP-43-positive aggregates in the cytosol (Fig. 3b). Irregular nuclear morphology with invaginated NMs was observed only in cells expressing APEX2-TDP-CTF or GFP-TDP-CTF (Fig. 3c).

To further investigate morphological deficits in the NM and NPCs, we used fluorescence microscopy on mouse primary cortical neurons expressing GFP or GFP-tagged TDP-CTF, TDP-43[WT], ALS-linked mutants (TDP-43[Q331K] and TDP-43[M337V]) or an NLS mutant (TDP-43[mtNLS]). Aggregated and mutant TDP-43 caused cytoplasmic mislocalization and/or aggregation of endogenous FG-Nups concomitant with morphological abnormalities in the NM stained with anti-lamin B antibody (Fig. 4a). A total of 43% of TDP-CTF-expressing cells and 29 to 36% of mutant TDP-43–expressing cells exhibited abnormal lamin B staining (Fig. 4b). 3D reconstruction of nuclei stained with anti-lamin B antibody further confirmed the deep invaginations of the NM in the presence of TDP-CTF aggregates (Supplementary Fig. 9a and Supplementary Videos 1

and 2). Knockdown of TDP-43 did not cause obvious NM defects in our primary neuron model (Fig. 4c), whereas morphological nuclear defects were previously reported in the TDP-43-depleted HeLa cells[21]. While this could be caused by a very severe reduction (>90%) of this essential RNA-binding protein leading to increased apoptosis, a dual gain- and loss-of-function mechanism leading to NM defects cannot be excluded. Abnormal RanGAP1 staining was observed only in the cells expressing TDP-CTF or TDP-43[mtNLS] (Fig. 4d and Supplementary Fig. 9b).

To clearly resolve the distribution of NPCs under normal and pathological conditions, we employed super-resolution structured-illumination microscopy (SIM). We found severely disturbed Nup98 distribution in the NM of N2a cells expressing GFP-TDP-CTF, with signs of NPC clustering in some parts of the NM (Fig. 4e). These strong defects in the nuclear morphology and the localization of Nups and TFs caused by aggregated or mutant TDP-43 suggested a consequential effect on nucleocytoplasmic transport processes.

The nuclear lamina helps maintain nuclear morphology, anchor NPCs, organize chromatin and trigger DNA repair[22]. We found that the impaired lamina structure in TDP-CTF-expressing neurons was associated with increased immunoreactivity for γH2AX, a marker for DNA double-strand breaks (Fig. 4f). There was a modest but significant difference between TDP-CTF and TDP-43[WT] (1.7-fold increase) or TDP-43[Q331K] (1.5-fold increase). Laminopathy-related DNA damage has also been observed in Alzheimer's disease with tau pathology[23], suggesting that lamin dysfunction may be frequently associated with neurodegeneration. To anchor the nuclear lamina to the inner NM, lamins are tethered to the cytoskeleton through the LINC (linkers of nucleoskeleton and cytoskeleton) complex[24,25]. We found that expression of TDP-CTF and TDP-43[Q331K] caused the mislocalization of the LINC proteins sun2 and nesprin-2, as well as a loss of F-actin integrity in cortical neurons (Supplementary Fig. 9c–f). These data suggest that TDP-43 pathology causes the disruption of the nuclear lamina by interfering with the structural support from LINC complex proteins and the peripheral cytoskeleton.

TDP-43 pathology disrupts nuclear import of proteins and export of mRNA. To examine nuclear protein import, we coexpressed GFP or GFP-TDP-43 with a fluorescent reporter protein flanked by NES and NLS sequences (NES-tdTomato-NLS) in primary cortical neurons. Quantitative analysis revealed a significant reduction of the nuclear-to-cytoplasmic (N-to-C) ratio of the reporter in cells expressing TDP-CTF or TDP-43 mutants compared to GFP control (Fig. 4g,h), indicating the cytoplasmic accumulation of reporter protein in the cells. Treatment with the nuclear import inhibitor importazole reduced the N-to-C ratio of the reporter to a similar degree, whereas staurosporine-induced apoptosis did not, thus ruling out the possibility that the observed protein import defects were caused by cell death (Fig. 4i). We also found that short hairpin RNA–mediated reduction of TDP-43 lowered the N-to-C ratio of reporter (Fig. 4j). However, the N-to-C ratio of Ran was not obviously affected by TDP-43 (Fig. 4k). Compared to TDP-43[WT], a significant reduction of the N-to-C ratio of TDP-43 and increases in cytoplasmic TDP-43 levels for TDP-43[M337V] and TDP-43[mtNLS] (TDP-43[M337V]/TDP-43[WT]: 1.3-fold, TDP-43[mtNLS]/TDP-43[WT]: 4.3-fold) were also observed (Supplementary Fig. 10a–c). The moderate but significant correlation of the N-to-C ratio of reporter to the N-to-C ratio of TDP-43 and the cytoplasmic TDP-43 levels (Supplementary Fig. 10d–f) suggest that subcellular TDP-43 levels need to be tightly regulated and that a relative increase in cytoplasmic TDP-43 levels may compromise nuclear protein import. To investigate whether TDP-43 pathology affects nuclear RNA export, we quantified poly(A) RNA levels in both nucleus and cytoplasm. Expression of TDP-CTF and TDP-43 mutants caused nuclear retention of poly(A) RNA, indicating impaired nuclear RNA export (Fig. 4l,m
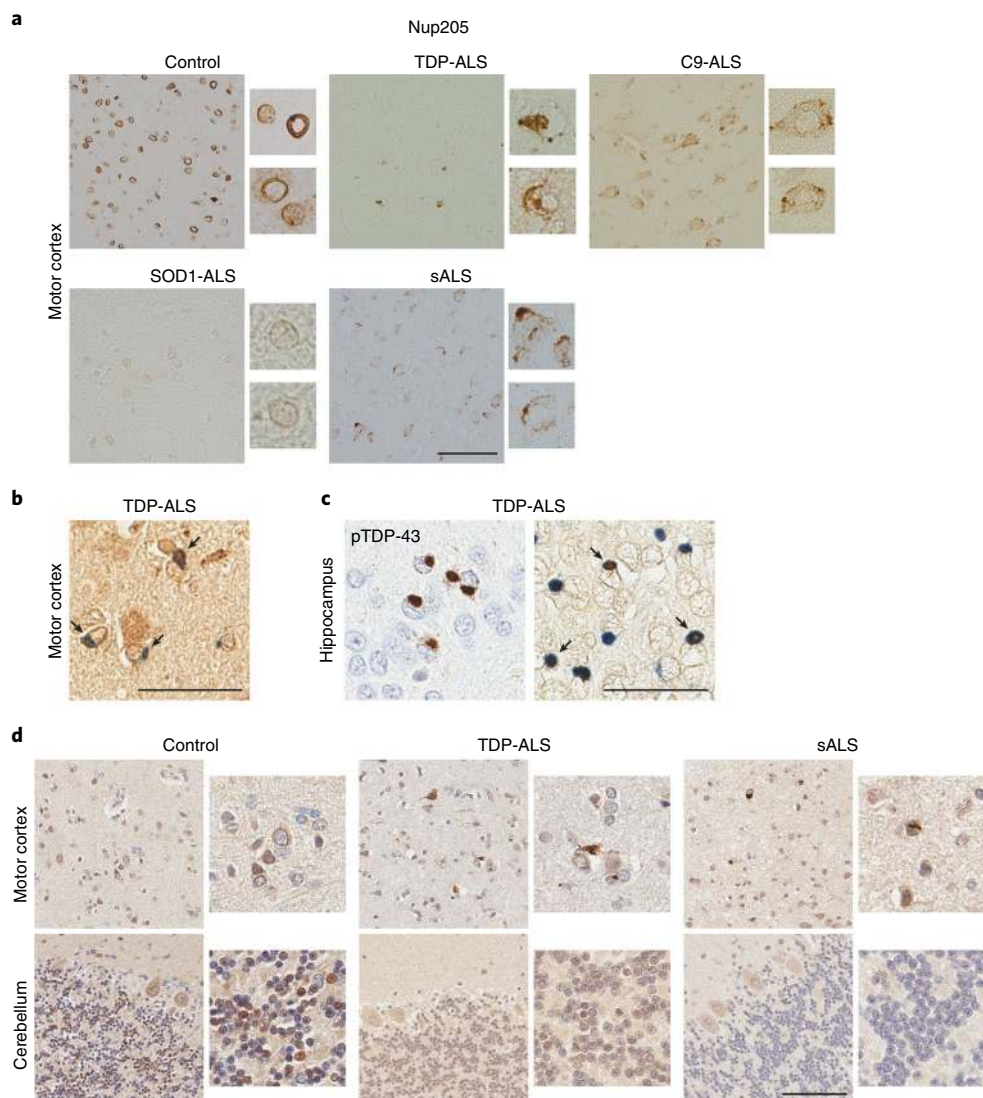
Fig. 7 | Nuclear pore pathology is present in fALS and sALS brain tissue with pTDP-43-positive inclusions. a, Immunohistochemical staining of Nup205 in human motor cortex was done once on samples from five control, ten sALS, seven C9-ALS, one SOD1-ALS and two TDP-ALS subjects, with similar results within groups. Scale bar: 100 μm. **b**, Double staining for pTDP-43 (blue) and Nup205 (brown) in motor cortex of TDP-ALS. Arrow indicates colocalization. Scale bar: 50 μm. **c**, pTDP-43 staining (left) and double staining of pTDP-43 (blue) and Nup205 (brown) (right) in TDP-ALS hippocampus. Arrow indicates colocalization. Scale bar: 50 μm. **d**, Immunohistochemical staining of Nup205 in motor cortex and cerebellum was done once on five control, five sALS and the TDP-ALS cases, with similar results within groups. Scale bar: 100 μm.

and Supplementary Fig. 10g). As a likely consequence of this defect, we observed a significant reduction of steady-state levels of protein translation in cells expressing TDP-43^{WT} or TDP-CTF, as measured by metabolic labeling of newly synthesized proteins (Fig. 4n).

We next assessed the effect of TDP-43 pathology at the endogenous levels in fibroblasts from three (per group) sALS, TDP-ALS and *C9orf72* mutation-associated ALS (C9-ALS) and healthy control subjects. Super-resolution imaging revealed evenly distributed FG-Nups and round-shaped lamin B staining in controls, while clustered FG-Nups and irregular and fragmented lamin B staining were present in TDP-ALS (Fig. 5a). γH2AX immunoreactivity increased by 1.6-fold in TDP-ALS compared to control (Fig. 5b). The distribution pattern of Nup205 was altered in C9-ALS and TDP-ALS fibroblasts, which exhibited significantly increased abnormal lamin B staining (17% and 22%), whereas sALS cells showed a trend for increase (Fig. 5c,d). Quantitative analysis further showed a significant reduction of the N-to-C ratio of reporter (Fig. 5e,f) and nuclear retention of poly(A) RNA (Fig. 5g,h) in ALS samples. Induced pluripotent

stem cell (iPSC)-derived motor neurons from healthy control and TDP-ALS showed significant increases in the percentage of TDP-ALS cells with mislocalized FG-Nups and distorted lamin B with increased immunoreactivity (Fig. 5i,j). These data suggest that the defects in the nucleocytoplasmic transport pathway are consistently observed in cortical neurons with ectopic expression of aggregated or mutant TDP-43, in fibroblasts and iPSC-derived neurons from subjects with ALS, as well as in a mechanistic ALS mouse model[26]. The dysregulation of nucleocytoplasmic shuttling and disruption of the NM and NPCs may be a common mechanism in both sALS and familial ALS (fALS) exhibiting TDP-43 proteinopathy.

Mutations in several *Nup* genes act as suppressors of TDP-43 toxicity in *Drosophila* models of ALS. To identify genetic interactions between TDP-43 toxicity and Nup function in vivo, we tested whether mutations in *Nup* genes could alter TDP-43 toxicity in *Drosophila* disease models for ALS. Expression of mutant TDP-43 in *Drosophila* motor neurons caused abnormal nuclear morphology[27] similar to
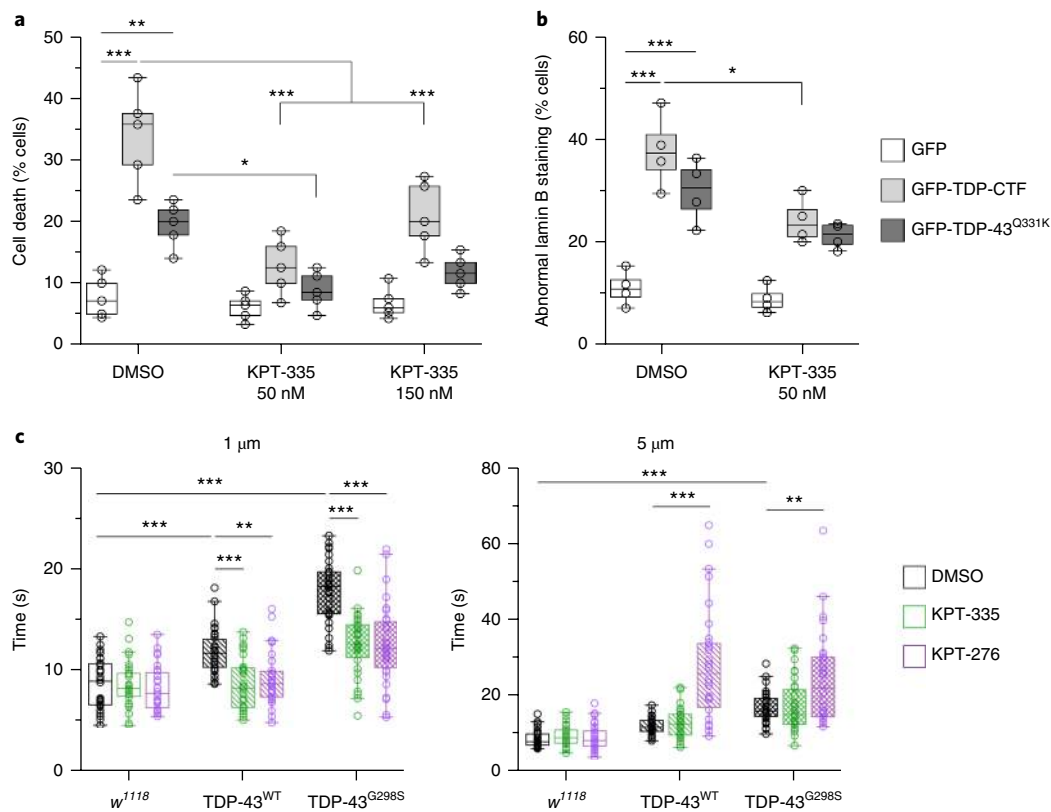
Fig. 8 | Pharmacological inhibition of TDP-43 toxicity rescues nucleocytoplasmic transport function caused by TDP-43 pathology. a, Overexpression of TDP-CTF or mutant TDP-43^{Q331K} increases cell death in transfected cortical neurons compared to GFP. Treatment with 50 nM KPT-335 for 24 hrs reduced cell death in both TDP-CTF and TDP-43^{Q331K}. **b**, Abnormal nuclear morphology with lamin B staining in neurons expressing TDP-CTF or TDP-43^{Q331K} is rescued by treatment with 50 nM KPT-335. **c**, Locomotion defects in larvae expressing human TDP-43^{WT} and TDP-43^{G298S} are ameliorated by treatment with 1 μM but not 5 μM PT-335 or KPT-276. Graphs represent quartiles (boxes), 50th percentiles (center lines) and range (whiskers). Five independent experiments for **a** (circles represent each independent experiment; *$P < 0.05$, **$P < 0.01$, ***$P < 0.001$, two-way ANOVA), four independent experiments for **b** (circles represent each independent experiment; *$P < 0.05$, ***$P < 0.001$, two-way ANOVA) and **c** (circles represent $n = 30$ animals; **$P < 0.01$, ***$P < 0.001$, two-way ANOVA). Bonferroni's post hoc test. Full statistical details are provided in Supplementary Table 4.

that found in spinal motor neurons of ALS patients[28]. Overexpression of human TDP-43^{WT} or TDP-43^{G298S} led to retinal degeneration and larval motor dysfunction (Fig. 6a,b). In addition to a *Nup50* mutation previously implicated as a genetic suppressor of TDP-43 toxicity[29], we identified several loss-of-function mutations in *Nup* genes that suppressed TDP-43-mediated eye phenotypes, including *Nup93*, *Nup98-96*, *Nup107* and *Nup214* (Fig. 6a). In larval turning assays, these mutations also rescued the locomotor dysfunction caused by TDP-43^{WT} or TDP-43^{G298S} expression in motor neurons (Fig. 6b). The results show that at least some aspects of TDP-43 toxicity in vivo depend on the nucleocytoplasmic transport machinery.

Nuclear pore pathology is common in ALS patient brain tissue with TDP-43 proteinopathy. We next investigated the presence of nuclear pore pathology in patient brain tissue with pTDP-43-positive inclusions, including subjects with sALS, TDP-ALS and C9-ALS (Supplementary Fig. 11a and Supplementary Table 2). To investigate the connection between TDP-43 and Nup pathology, we also stained the motor cortex from one subject with SOD1-associated ALS (SOD1-ALS) and cerebellum from subjects with TDP-ALS and sALS, which acted as pTDP-43-negative controls (Supplementary Fig. 11b). Indeed, in the motor cortex, TDP-ALS and sALS tissues but not age-matched controls showed a widespread loss of Nup205 immunoreactivity and large Nup205-positive cytoplasmic inclusions, whereas neurons in C9-ALS tissues exhibited abnormal perinuclear punctate staining (Fig. 7a). We found colocalization

of Nup205 with pTDP-43-posive-inclusions in the motor cortex and more frequently in the hippocampus in TDP-ALS, suggesting partial coaggregation (Fig. 7b,c). Cytoplasmic Nup205-positive inclusions were also observed in the frontal cortex in ALS (Supplementary Fig. 12). However, neither the SOD1-ALS motor cortex nor any cerebellum exhibited Nup205 pathology (Fig. 7a,d). Notably, samples from one of the two subjects with TDP-ALS showed no pTDP-43-positive inclusions in the motor cortex[30] and were also devoid of Nup205 pathology. Abnormal NM morphology was occasionally present in the motor cortex in TDP-ALS but scarcely found in C9-ALS and sALS (Supplementary Fig. 13). However, we did not observe obvious defects in RanGAP1 staining among our cohort (Supplementary Fig. 14). These data show that nuclear pore pathology may be a histopathological hallmark of fALS and sALS in the presence of TDP-43 proteinopathy, even in the absence of *C9orf72* repeat expansion.

Suppression of TDP-43 toxicity rescues nucleocytoplasmic transport defects in vitro and in vivo. To assess pharmacological rescue of nucleocytoplasmic transport defects in TDP-43 pathology, we used a selective inhibitor, KPT-335 (verdinexor), which interferes with the Xpo1/Crm1-dependent nuclear export pathway. KPT-335 was reported to inhibit influenza virus[31] and TNF-α neurotoxicity[32]. The related compound KPT-276 has previously shown neuroprotection in C9-ALS[33], and KPT-350 has done so in Huntington's disease[34]. We have previously shown that aggregated and mutant

TDP-43 increases neurotoxicity in primary cortical neurons[10]. Treatment with 50 nM KPT-335 significantly suppressed 55 to 62% of cell death caused by TDP-CTF or TDP-43^{Q331K} in cortical neurons, whereas 150 nM KPT-335 resulted in a trend for increased toxicity (Fig. 8a). The defects in nuclear morphology caused by TDP-CTF were also rescued by the treatment with 50 nM KPT-335 (Fig. 8b). Larval locomotor defects caused by human TDP-43^{WT} or TDP-43^{G298S} were also ameliorated by treatment with 1 µM but not 5 µM KPT-276 or KPT-335 (Fig. 8c).

Previously, we had identified poly(A)-binding protein nuclear 1 (PABPN1) as a potent suppressor of TDP-43 toxicity and aggregation that acts via a proteasome-dependent mechanism[10]. To assess its ability to rescue nucleocytoplasmic transport defects, we coexpressed TDP-CTF with PABPN1 in cortical neurons. PABPN1 overexpression not only led to the clearance of soluble and insoluble TDP-CTF (Supplementary Fig. 15a), but also restored the proper localization of endogenous FG-Nups and lamin B (Supplementary Fig. 15b,c). TDP-CTF-mediated defects in nuclear protein import (Supplementary Fig. 15d) and mRNA export (Supplementary Fig. 15e) were also rescued. These results suggest that suppression of TDP-43 toxicity via pharmacological or molecular inhibition may be a valid strategy for rescuing the defective nucleocytoplasmic transport function.

Discussion

Here we have established a modified BioID procedure as a method to interrogate the proteome of insoluble aggregates associated with neurodegenerative diseases. Our study provides evidence that (1) proteins involved in nucleocytoplasmic transport are major components of pathological TDP-43 aggregates, (2) aggregated and mutant TDP-43 cause cytoplasmic mislocalization and/or aggregation of Nups and TFs, (3) PrLDs present in human Nups containing FG repeats are required and sufficient for coaggregation, (4) aggregated and mutant TDP-43 trigger morphological defects in the NM and NPCs, as well as functional defects in nuclear protein import and mRNA export, (5) several *Nup* genes act as genetic modifiers of TDP-43 toxicity in *Drosophila*, (6) pharmacological and molecular inhibition of TDP-43 toxicity rescue nucleocytoplasmic transport defects and (7) nuclear pore pathology is present in motor and frontal cortex in sALS and fALS with pTDP-43-positive inclusions, suggesting that defective nucleocytoplasmic transport represents a common neuropathological hallmark in ALS and potentially other TDP-43 proteinopathies.

The specific composition of TDP-43 aggregates has remained unknown, perhaps due to technical limitations in preserving protein interactions under the harsh lysis conditions required for the extraction of insoluble aggregates. To address this question, we adapted a method for proximity-based biotinylation of proteins for the characterization of pathological aggregates[12,13]. The high affinity of streptavidin and neutravidin for biotin allowed us to purify biotinylated proteins under the strong denaturing condition required for solubilizing protein aggregates. Robust labeling of proteins in detergent-insoluble aggregates suggests that this method has a broad applicability for the study of a wide range of neuropathological inclusions. Our proteomic analysis of pathological TDP-43 aggregates led to the unexpected discovery that cytoplasmic TDP-43 aggregates are highly enriched for components of NPCs, as well as TFs. Our findings imply that TDP-43 may not only be mislocalized as a consequence of defects in nucleocytoplasmic transport, but also directly inhibit the nuclear import and export of macromolecules by sequestering components in this pathway. In addition, proteins involved in vesicular trafficking between endoplasmic reticulum and Golgi were also enriched in the TDP-CTF interactome (Supplementary Fig. 2). Of note, endoplasmic reticulum–Golgi transport dysfunction was found associated with various ALS mutations[35]. TDP-43 mutation had also been reported to compromise axonal mRNA transport in human motor neurons[36], suggesting that deficits in multiple intracellular trafficking could be linked to the pathogenesis of ALS/FTD.

Although pathogenic mechanisms related to Nups have been widely studied in a variety of diseases[37], little is known about their role in neurodegeneration. The first evidence related to ALS addressed a loss of Kpnb1 immunoreactivity and ruffled nuclear morphology upon staining with Nup62 and Nup153 antibodies in spinal motor neurons in sALS[28]. Mutations in the *Gle1* gene, encoding an essential RNA export factor, were found to be associated with ALS and cause a deficit in motor neuron development in zebrafish upon its loss of function[38]. Notably, several recent studies have linked ALS/FTD caused by an intronic G$_4$C$_2$ hexanucleotide repeat expansion in the *C9orf72* locus to nucleocytoplasmic transport defects. Expression of 30 G$_4$C$_2$ repeats resulted in retinal degeneration in a *Drosophila* model of C9-ALS. One of the proposed mechanisms was the sequestration of RanGAP1 into G$_4$C$_2$ RNA foci, which interfered with Ran-dependent nucleocytoplasmic transport[33]. Additionally, unbiased genetic screens identified components of the nucleocytoplasmic transport machinery as genetic modifiers of *C9orf72* toxicity in *Drosophila* expressing (G$_4$C$_2$)$_{58}$ and in yeast expressing poly(Pro-Arg)$_{50}$[39,40]. Poly(Gly-Ala) forms intracellular aggregates that were found to sequester nuclear pore proteins, such as Pom121, in a new C9-ALS mouse model[41]. Additionally, several Nups, such as Pom121 and Nup107, are very long-lived proteins in postmitotic cells and susceptible to oxidative insults. The poor turnover of damaged Nups as well as age-dependent decline of TFs may result in irreversible neuronal dysfunction and death[42,43]. Taken together, these studies suggest that defects in the nucleocytoplasmic transport machinery may be central to the pathogenesis of C9-ALS.

Notably, several of these studies suggest that defects in nuclear transport leads to TDP-43 cytoplasmic mislocalization as a consequence. Ran has been identified as an essential regulator of TDP-43 nuclear localization[44]. The expression of (G$_4$C$_2$)$_{30}$ RNA impairs the NM morphology and reduces the N-to-C Ran gradient. The reduction of nuclear Ran was found to be correlated with the nuclear depletion of TDP-43 in C9-ALS iPSC-derived neurons and a *GRN* knockout mouse model[33,44]. The short interfering RNA–mediated reduction of Nup62, CAS or Kpnb1 levels also triggers cytoplasmic accumulation of TDP-43[45].

In this study, however, we show that TDP-43 pathology itself triggers structural defects in the NM and NPCs, with ensuing impairment of nucleocytoplasmic transport in mouse primary cortical neurons, as well as fibroblasts and iPSC-derived neurons from ALS patients. This is further supported by our observation of nuclear pore pathology in the brain tissues from pTDP-43-positive sALS and TDP-ALS but not those that are pTDP-43 negative. Altered nuclear morphology has also been observed in brain samples of TDP-43 transgenic mice and in human cases of frontotemporal lobar degeneration–TDP[46]. Our data suggest a common role for NM and NPC pathology in the disease mechanism of most ALS/FTD cases. A broader role for nucleocytoplasmic transport defects in age-dependent neurodegeneration is further supported by the finding that the cytoplasmic aggregation of artificial β-sheet proteins, as well as fragments of mutant huntingtin and TDP-43, can interfere with mRNA export in HEK293T cells and mouse primary cortical neurons. This deficit may result from mislocalization of a subunit of the THO complex (THOC2), which is involved in mRNA export[47]. Notably, cytoplasmic but not nuclear β-sheet protein triggers cellular toxicity and the mislocalization of nuclear transport factors and poly(A) RNA. Notably, an altered localization of Nups and TFs and nucleocytoplasmic transport function was also found as an age-dependent phenotype in a mutant huntingtin knock-in mouse model and Huntington's disease patients[34,48]. These results suggest that several disease-associated protein aggregates can impair the NPC integrity and nucleocytoplasmic transport function. However, how protein

aggregates in distinct compartments share a similar pathogenic mechanism in various diseases remains to be investigated in detail.

As a possible mechanistic explanation, we have identified PrLDs and low-complexity domains similar to those frequently found in RNA-binding proteins within FG-rich domains of several human Nups. These domains were both required and sufficient for coaggregation with TDP-CTF. Notably, the arginine-rich dipeptide repeats, including poly(Pro-Arg) and poly(Gly-Arg), can interact with membraneless organelles, such as nucleoli, NPCs and stress granules, through the low-complexity domains and disrupt organelle function and dynamics[49]. The sorting capability of NPCs is driven by the phase separation of FG domains into dense and sieve-like hydrogels. A similar phase separation process driven by low-complexity domains has also been recognized in stress granule formation and the pathological transition to insoluble aggregates, making this process an important emerging principle in neurodegeneration[50]. Our findings suggest that the interaction of PrLDs in TDP-43 and those in FG-Nups may trigger the pathological cascade in a similar way.

We found that many Nups and TFs were affected by TDP-43 pathology. Notably, some components of the nucleocytoplasmic transport machinery were not affected, but instead prevented the cytoplasmic aggregation of TDP-CTF. The most pronounced effect was found for Kpnb1, which is involved in nuclear import in concert with NLS-binding Kpna proteins. A previous screen of 82 proteins involved in nuclear transport found that downregulation of Kpnb1 causes cytoplasmic accumulation of TDP-43[45].

Here we identified several genetic suppressors in our fly system. Among these, *Nup98-96* and *Nup107* mutations have been previously shown to reduce G$_4$C$_2$-mediated toxicity[39]. In a search for candidate genes near the gene locus of *Hey*, a *Nup50* mutation was found to rescue the lifespan of TDP-43 transgenic flies[29]. The reduced expression of *Nup* genes may compensate the defects in nucleocytoplasmic transport and ameliorate TDP-43 toxicity by reducing cytoplasmic shuttling of TDP-43. We also found that pharmacological treatment with the selective nuclear export inhibitors KPT-276 and KPT-335 rescued TDP-43 toxicity and defective nucleocytoplasmic transport function in cortical neurons and *Drosophila*, similarly to its effect in C9-ALS models[33], suggesting a potential therapeutic application in most ALS cases.

Taken together, our data suggest that the disruption of the NM and NPCs and nucleocytoplasmic transport function may be a common pathogenesis in most ALS and most FTD with TDP-43 proteinopathy. Based on our findings, we propose that (1) cytoplasmic mislocalization of TDP-43 due to nucleocytoplasmic transport defects caused by the *C9orf72* repeat expansion can exacerbate these defects in a positive feedback loop, and (2) cytoplasmic accumulation of TDP-43 can directly trigger nucleocytoplasmic transport defects by disrupting the localization of Nups and TFs (Supplementary Fig. 16). A better understanding of the role of TDP-43 in intracellular transport pathways may help in developing therapeutic strategies for ALS/FTD and other TDP-43 proteinopathies.

Methods

References

1. Ling, S. C., Polymenidou, M. & Cleveland, D. W. Converging mechanisms in ALS and FTD: disrupted RNA and protein homeostasis. *Neuron* **79**, 416–438 (2013).
2. Neumann, M. et al. Ubiquitinated TDP-43 in frontotemporal lobar degeneration and amyotrophic lateral sclerosis. *Science* **314**, 130–133 (2006).
3. Igaz, L. M. et al. Enrichment of C-terminal fragments in TAR DNA-binding protein-43 cytoplasmic inclusions in brain but not in spinal cord of frontotemporal lobar degeneration and amyotrophic lateral sclerosis. *Am. J. Pathol.* **173**, 182–194 (2008).
4. Buratti, E. et al. TDP-43 binds heterogeneous nuclear ribonucleoprotein A/B through its C-terminal tail: an important region for the inhibition of cystic fibrosis transmembrane conductance regulator exon 9 splicing. *J. Biol. Chem.* **280**, 37572–37584 (2005).
5. Gitcho, M. A. et al. TDP-43 A315T mutation in familial motor neuron disease. *Ann. Neurol.* **63**, 535–538 (2008).
6. Nonaka, T., Kametani, F., Arai, T., Akiyama, H. & Hasegawa, M. Truncation and pathogenic mutations facilitate the formation of intracellular aggregates of TDP-43. *Hum. Mol. Genet.* **18**, 3353–3364 (2009).
7. Guo, W. et al. An ALS-associated mutation affecting TDP-43 enhances protein aggregation, fibril formation and neurotoxicity. *Nat. Struct. Mol. Biol.* **18**, 822–830 (2011).
8. Li, Y. R., King, O. D., Shorter, J. & Gitler, A. D. Stress granules as crucibles of ALS pathogenesis. *J. Cell Biol.* **201**, 361–372 (2013).
9. Fallini, C., Bassell, G. J. & Rossoll, W. The ALS disease protein TDP-43 is actively transported in motor neuron axons and regulates axon outgrowth. *Hum. Mol. Genet.* **21**, 3703–3718 (2012).
10. Chou, C. C. et al. PABPN1 suppresses TDP-43 toxicity in ALS disease models. *Hum. Mol. Genet.* **24**, 5154–5173 (2015).
11. Igaz, L. M. et al. Expression of TDP-43 C-terminal fragments in vitro recapitulates pathological features of TDP-43 proteinopathies. *J. Biol. Chem.* **284**, 8516–8524 (2009).
12. Roux, K. J., Kim, D. I., Raida, M. & Burke, B. A promiscuous biotin ligase fusion protein identifies proximal and interacting proteins in mammalian cells. *J. Cell Biol.* **196**, 801–810 (2012).
13. Kim, D. I. et al. Probing nuclear pore complex architecture with proximity-dependent biotinylation. *Proc. Natl. Acad. Sci. USA* **111**, E2453–E2461 (2014).
14. Rout, M. P. et al. The yeast nuclear pore complex: composition, architecture, and transport mechanism. *J. Cell Biol.* **148**, 635–651 (2000).
15. Lim, L., Wei, Y., Lu, Y. & Song, J. ALS-causing mutations significantly perturb the self-assembly and interaction with nucleic acid of the intrinsically disordered prion-like domain of TDP-43. *PLoS Biol.* **14**, e1002338 (2016).
16. Wright, P. E. & Dyson, H. J. Intrinsically disordered proteins in cellular signalling and regulation. *Nat. Rev. Mol. Cell Biol.* **16**, 18–29 (2015).
17. Halfmann, R., Wright, J. R., Alberti, S., Lindquist, S. & Rexach, M. Prion formation by a yeast GLFG nucleoporin. *Prion* **6**, 391–399 (2012).
18. Frey, S. & Görlich, D. A saturated FG-repeat hydrogel can reproduce the permeability properties of nuclear pore complexes. *Cell* **130**, 512–523 (2007).
19. Kato, M. et al. Cell-free formation of RNA granules: low complexity sequence domains form dynamic fibers within hydrogels. *Cell* **149**, 753–767 (2012).
20. Lam, S. S. et al. Directed evolution of APEX2 for electron microscopy and proximity labeling. *Nat. Methods* **12**, 51–54 (2015).
21. Ayala, Y. M., Misteli, T. & Baralle, F. E. TDP-43 regulates retinoblastoma protein phosphorylation through the repression of cyclin-dependent kinase 6 expression. *Proc. Natl. Acad. Sci. USA* **105**, 3785–3789 (2008).
22. Broers, J. L., Ramaekers, F. C., Bonne, G., Yaou, R. B. & Hutchison, C. J. Nuclear lamins: laminopathies and their role in premature ageing. *Physiol. Rev.* **86**, 967–1008 (2006).
23. Frost, B., Bardai, F. H. & Feany, M. B. Lamin dysfunction mediates neurodegeneration in tauopathies. *Curr. Biol.* **26**, 129–136 (2016).
24. Crisp, M. et al. Coupling of the nucleus and cytoplasm: role of the LINC complex. *J. Cell Biol.* **172**, 41–53 (2006).
25. Zhang, Q. et al. Nesprin-1 and -2 are involved in the pathogenesis of Emery Dreifuss muscular dystrophy and are critical for nuclear envelope integrity. *Hum. Mol. Genet.* **16**, 2816–2833 (2007).
26. Yamashita, T., Aizawa, H., Teramoto, S., Akamatsu, M. & Kwak, S. Calpain-dependent disruption of nucleo-cytoplasmic transport in ALS motor neurons. *Sci. Rep.* **7**, 39994 (2017).
27. Estes, P. S. et al. Motor neurons and glia exhibit specific individualized responses to TDP-43 expression in a *Drosophila* model of amyotrophic lateral sclerosis. *Dis. Model. Mech.* **6**, 721–733 (2013).
28. Kinoshita, Y. et al. Nuclear contour irregularity and abnormal transporter protein distribution in anterior horn cells in amyotrophic lateral sclerosis. *J. Neuropathol. Exp. Neurol.* **68**, 1184–1192 (2009).
29. Zhan, L., Hanson, K. A., Kim, S. H., Tare, A. & Tibbetts, R. S. Identification of genetic modifiers of TDP-43 neurotoxicity in *Drosophila*. *PLoS One* **8**, e57214 (2013).
30. Cairns, N. J. et al. TDP-43 proteinopathy in familial motor neurone disease with TARDBP A315T mutation: a case report. *Neuropathol. Appl. Neurobiol.* **36**, 673–679 (2010).
31. Perwitasari, O. et al. Antiviral efficacy of verdinexor in vivo in two animal models of influenza a virus infection. *PLoS One* **11**, e0167221 (2016).
32. Tajiri, N. et al. A Nuclear attack on traumatic brain injury: sequestration of cell death in the nucleus. *CNS Neurosci. Ther.* **22**, 306–315 (2016).

33. Zhang, K. et al. The C9orf72 repeat expansion disrupts nucleocytoplasmic transport. *Nature* **525**, 56–61 (2015).
34. Grima, J. C. et al. Mutant huntingtin disrupts the nuclear pore complex. *Neuron* **94**, 93–107.e6 (2017).
35. Soo, K. Y. et al. Rab1-dependent ER-Golgi transport dysfunction is a common pathogenic mechanism in SOD1, TDP-43 and FUS-associated ALS. *Acta Neuropathol.* **130**, 679–697 (2015).
36. Alami, N. H. et al. Axonal transport of TDP-43 mRNA granules is impaired by ALS-causing mutations. *Neuron* **81**, 536–543 (2014).
37. Nofrini, V., Di Giacomo, D. & Mecucci, C. Nucleoporin genes in human diseases. *Eur. J. Hum. Genet.* **24**, 1388–1395 (2016).
38. Kaneb, H. M. et al. Deleterious mutations in the essential mRNA metabolism factor, hGle1, in amyotrophic lateral sclerosis. *Hum. Mol. Genet.* **24**, 1363–1373 (2015).
39. Freibaum, B. D. et al. GGGGCC repeat expansion in C9orf72 compromises nucleocytoplasmic transport. *Nature* **525**, 129–133 (2015).
40. Jovičić, A. et al. Modifiers of C9orf72 dipeptide repeat toxicity connect nucleocytoplasmic transport defects to FTD/ALS. *Nat. Neurosci.* **18**, 1226–1229 (2015).
41. Zhang, Y. J. et al. C9ORF72 poly(GA) aggregates sequester and impair HR23 and nucleocytoplasmic transport proteins. *Nat. Neurosci.* **19**, 668–677 (2016).
42. Pujol, G., Söderqvist, H. & Radu, A. Age-associated reduction of nuclear protein import in human fibroblasts. *Biochem. Biophys. Res. Commun.* **294**, 354–358 (2002).
43. D'Angelo, M. A., Raices, M., Panowski, S. H. & Hetzer, M. W. Age-dependent deterioration of nuclear pore complexes causes a loss of nuclear integrity in postmitotic cells. *Cell* **136**, 284–295 (2009).
44. Ward, M. E. et al. Early retinal neurodegeneration and impaired Ran-mediated nuclear import of TDP-43 in progranulin-deficient FTLD. *J. Exp. Med.* **211**, 1937–1945 (2014).
45. Nishimura, A. L. et al. Nuclear import impairment causes cytoplasmic trans-activation response DNA-binding protein accumulation and is associated with frontotemporal lobar degeneration. *Brain* **133**, 1763–1771 (2010).
46. Amlie-Wolf, A. et al. Transcriptomic changes due to cytoplasmic TDP-43 expression reveal dysregulation of histone transcripts and nuclear chromatin. *PLoS One* **10**, e0141836 (2015).
47. Woerner, A. C. et al. Cytoplasmic protein aggregates interfere with nucleocytoplasmic transport of protein and RNA. *Science* **351**, 173–176 (2016).
48. Gasset-Rosa, F. et al. Polyglutamine-expanded huntingtin exacerbates age-related disruption of nuclear integrity and nucleocytoplasmic transport. *Neuron* **94**, 48–57.e4 (2017).
49. Lee, K. H. et al. C9orf72 dipeptide repeats impair the assembly, dynamics, and function of membrane-less organelles. *Cell* **167**, 774–788.e17 (2016).
50. Molliex, A. et al. Phase separation by low complexity domains promotes stress granule assembly and drives pathological fibrillization. *Cell* **163**, 123–133 (2015).

Acknowledgements

Author contributions

W.R. conceived and directed the project. C.-C.C., Y.Z. and W.R. designed the experiments. C.-C.C. and W.R. interpreted data and wrote the manuscript. C.-C.C. characterized protein interactome, performed bioinformatic analysis and conducted experiments in N2a cells, primary cortical neurons and human fibroblasts with help from F.L. and Y.H.C. Y.Z. performed the BioID pulldown and sample preparation for LC-MS/MS analysis. M.E.U. performed immunohistochemistry staining. S.W.V., M.S. and D.C.Z. performed *Drosophila* experiments. I.L. and R.S. performed experiments in iPSC-derived motor neurons. C.-C.C. and P.G.D.-A. conducted SIM experiments. D.M.D., N.T.S. and M.A.P. provided technical support. T.K. provided key reagents. C.M.H., M.G., N.J.C., K.B.B., D.W.D., R.R., Y.-J.Z., L.P. and J.D.G. provided patient tissue with associated clinical and genetics data.

Competing interests

The authors declare that they have no competing financial interests.

Additional information

Supplementary information is available for this paper at https://doi.org/10.1038/s41593-017-0047-3.

Reprints and permissions information is available at www.nature.com/reprints.

Correspondence and requests for materials should be addressed to W.R.

Publisher's note: Springer Nature remains neutral with regard to jurisdictional claims in published maps and institutional affiliations.

Methods

Constructs. The expression plasmids encoding nucleoporin (Nup) and nucleocytoplasmic transport factor (TF) fusion proteins are obtained from multiple sources (Supplementary Table 3). PCR-amplified human TDP-43 and TDP-CTF were cloned into the pcDNA3.1 myc-BioID vector (Addgene)[12] as XhoI/KpnI fragments and cloned from GFP expression plasmids into the Kpn2I/MluI sites of the APEX2-Actin plasmid (Addgene)[20]. TDP-CTF (aa 208–414) was generated by PCR, and Q331K, M337V and NLS (KRK….KVKR > AAA….AVAA)[51] mutations were generated by site-directed mutagenesis (QuikChange II, Agilent) and cloned into pEGFP-C1 (Clontech) or mCherry vector. A flexible linker [(SGGG)₃] was inserted between all the fusion partners to facilitate correct protein folding. PCR primers used to generate PrLD and non-PrLD fragments of Nup98:
5′-CAGATCTCCGGAGGCGGCTCCATGGAGATGTTTAACAAATCATTTGG-3′;
5′-ACAATTGCATCAACCTCCAGGCTGTGAGGCTTG-3′;
5′-CAGATCTCCGATGCTTTTTGGGACAGCTACAAACACC-3′;
5′-ACAATTGATTCACTGTCCTTTTTTCTCTACCTGAGG-3′.
PCR products were cloned into the BglII/MfeI sites of pEGFP-Nup98. PCR primers used to generate PrLD and non-PrLD fragments of Nup153: 5′-CGCTAGCTCTAGACTAGGGGACACCATGG-3′;
5′-GACCGGTGGTACAAAGGAGGATCCTGCAGAGCTAG-3′;
5′- CGCTAGCTCTAGACTAGGGGACACCATGTTTGGAACTGGAC
CCTCAGCACC-3′; 5′-GACCGGTGGTTTCCTGCGTCTAACAGC-3′.
PCR products were cloned into the NheI/AgeI sites of pNup153-EGFP. PCR primers used to generate PrLD and non-PrLD of Nup214:
5′-CAGATCTCCGGAGGCGGCGCGATGGGAGACGAGATGGATG-3′;
5′-ACAATTGCATCAGGCAGCTGCTGTGCTGGCTGTG-3′;
5′- CAGATCTCCGGAGGCGGCGCGATGAACCAACAGGTCAGCAGCTCAGG-3′;
5′-ACAATTGCCTCAGCTTCGCCAGCCACCAAAACCCTGG-3′. PCR products were cloned into pEGFP-Nup214 as BglII/MfeI fragments. GIPZ TDP-43 shRNA constructs (shTDP-43, V3LHS_636490) and a nonsilencing control (shCtrl, RHS4346) were obtained from Open Biosystems.

Drosophila genetics. All *Drosophila* stocks and crosses were maintained on standard yeast/cornmeal/molasses food at 22 °C. GAL4 drivers (GMR GAL4 for retinal expression and D42 GAL4 for motor neuron expression) were used to express human TDP-43 with C-terminal YFP tag as previously described[52]. For controls, w[1118] flies were crossed with the appropriate GAL4 driver. *Drosophila* lines harboring mutations in nuclear pore components were obtained from the Bloomington *Drosophila* Stock Center and have the following genotypes: y[1]; P{y[+mDint2] w[BR.E.BR] = SUPor-P}Nup50[KG09557]; ry[506], w[*] P{w[+mC] = EP}Nup93-1[G9996], Nup98-96[339]/TM3, Sb[1] and y[1] w[67c23]; P{y[+t7.7] w[+mC] = wHy}Nup107[DG40512]/SM6a. Both female and male adults were tested.

Adult eye imaging. Adult fly eyes were imaged with a Leica MZ6 microscope equipped with an Olympus DP73 camera and controlled by Olympus DP Controller and Olympus DP Manager software. Individual images were processed using Adobe Photoshop CS6 (Adobe).

Larval turning assays. Larval turning assays were performed as described[53]. Briefly, crosses were carried out at 22 °C and wandering third instar larvae were placed on a grape juice plate. After a short acclimation period, larvae were gently turned ventral side up. They were observed until they turned over (dorsal side up) and began making a forward motion. The time it took to complete this task was recorded.

For drug screening, UAS TDP-43 males were crossed with D42-GAL4 female virgins on fly food containing either DMSO, KPT-226 or KPT-335. For DMSO controls, the same volume of DMSO as the corresponding drug concentration was added. Crosses were made on drug food and maintained at 25 °C. Both female and male larvae were tested.

Cell culture and transfection. All procedures for animal experiments were approved by the Emory University Institutional Animal Care and Use Committee. Primary cortical neurons were isolated from cerebral cortex of mixed male and female C57BL/6 J mouse embryos at day 16.5 (E16.5) and cultured as previously described[54]. Briefly, cells were plated on coverslips coated with 0.5 mg/ml poly-L-ornithine (Sigma-Aldrich) for 2 h in MEM (Life Technologies) containing 10% FBS (Hyclone). After switching to complete neural cell culture medium (Neurobasal medium (Life Technologies), 1% Glutamax (Life Technologies) and 2% B-27 supplements (Life Technologies)), cells were cultured for 5 d. Neurons were transected via magnetofection with 0.5 µg plasmid DNA and 1.75 µL NeuroMag (Oz Biosciences) as described[55]. Cells were cultured for 24 h and processed for immunofluorescence. For TDP-43 knockdown, cells were transfected with expression plasmids for shCtrl or shTDP-43 and cultured for another 5 d to efficiently reduce TDP-43 protein levels[9]. Transfection efficiency was in the range of 20–30% for overexpression and 10–15% for TDP-43 knockdown experiments. shTDP-43 reduced TDP-43 protein levels to 61% of those in shCtrl-transfected cells.

Mouse Neuro-2a (N2a) neuroblastoma cells were plated in 6-well plates for immunoblotting or on coverslips in 12-well plates for immunofluorescence and

cultured in DMEM (Life Technologies) containing 10% FBS and 1% PenStrep (Sigma-Aldrich). Cells were transfected with either Lipofectamine 3000 (Life Technologies) or PolyMag Neo (Oz Biosciences) according to the manufacturer's protocol and the medium was changed the next day. Cells were fixed 48 h after transfection. Transfection efficiency was in the range of 70–80%. N2a cells were obtained from ATCC (CCL-131) and tested for mycoplasma contamination.

Collection of human fibroblasts was approved by the Emory and Mayo Clinic Institutional Review Boards, and informed consent for participation was obtained from every subject and/or an appropriate surrogate. Human fibroblasts from healthy control and ALS subjects were plated on coverslips coated with 0.5 mg/ml poly-L-ornithine in DMEM containing 10% FBS supplemented with 0.5% PenStrep, 1% MEM with nonessential amino acids (NEAA) (Life Technologies) and 55 µM 2-mercaptoethanol (Life Technologies).

Control and TDP-43 mutant iPSC lines were cultured and maintained in MTeSR medium (Stem Cell Technologies) in the presence of ROCK inhibitor. During the neuralization stage, cells were cultured for 2 d in WiCell Medium (DMEM/F12, knockout serum replacement, 1% L-glutamine, 1% NEAA, 110 µ M 2-mercaptoethanol) supplemented with 0.5 µM LDN (Stemgent) and 10 µM SB (Sigma) for BMP and SMAD pathway inhibition. To induce caudalization, cells were cultured for 5 d in 50% WiCell + 50% neural induction medium (NIM: DMEM/F12, 1% L-glutamine, 1% NEAA, 1% N2, 1% Pen/Strep and 2 µg/ml heparin) and supplemented with 0.5 µM LDN, 10 µM SB and 0.5 µM retinoic acid (RA) (Sigma). For ventralization, cells were cultured and maintained in NIM supplemented with 0.5 µM RA, 200 ng/ml SHH-C (Peprotech), 10 ng/ml BDNF (Invitrogen) and 0.4 µg/ml ASAC (Sigma) for 7 d. At the stage of neural progenitor cell differentiation, cells were cultured for 6 d in 50% NIM + 50% neural differentiation medium (NDM: Neurobasal, 1% L-glutamine, 1% NEAA, 1% N2, 1% Pen/Strep) and supplemented with 0.5 µM RA, 200 ng/ml SHH-C, 0.4 µg/ ml ASAC, 2% B27, 10 ng/ml BDNF, 10 ng/ml GDNF (R&D Systems), 10 ng/ml IGF (R&D Systems) and 10 ng/ml CNTF (R&D Systems). The medium was then changed to 100% NDM. On differentiation day 32, iPSC neurons were treated with 20 mM AraC (Sigma) for 48 h to remove glial progenitors cells. Ninety percent of cells were positive for the Tuj-1 neuronal marker and 30–40% of the cells were positive for the motor neuron marker HB9, as previously described[56]. For coculture of human iPSC-derived neurons with mouse astrocytes, starting at DIV40, differentiated neurons were cocultured on top of a confluent monolayer of mouse cortical astrocytes prepared from postnatal day 0–1 mouse pups. The cells were kept until DIV 54–57, when they were fixed for mAb414 and lamin B staining.

Affinity pulldown of biotinylated proteins and immunoblotting. N2a cells were transfected with expression plasmids for GFP, myc-BirA*-TDP-43 or myc-BirA*-TDP-CTF using Lipofectamine 3000. The culture medium was changed after 4 h and, the next day, biotin was added to the medium at 50 µM. After 24 h, cells were harvested and washed with cold PBS three times before cell lysis in urea buffer (8 M urea, 50 mM Tris-HCl pH 7.5) supplemented with protease inhibitor (Roche) and phosphatase inhibitor (Roche) for 20 min at room temperature (RT) with occasional vortexing. Cells were sonicated three times in 2-s pulses and centrifuged at 20,000 g at RT for 15 min. A small aliquot from the supernatant (input sample) was mixed with Laemmli buffer and boiled for 5 min. For the pulldown of biotinylated proteins, neutravidin beads (Thermo Fisher Scientific) were prewashed with lysis buffer and incubated with the remaining lysate sample with constant rotation overnight at RT. Beads were collected by centrifugation and washed five times with lysis buffer. Twenty percent of the sample was reserved for immunoblotting and 80% was used for mass spectrometry (Fig. 1b,d).

Immunoblotting was performed according to standard protocols. Samples mixed with Laemmli buffer were heated for 5 min at 98 °C and spun down before running on a 10% SDS–PAGE gel and electrotransfer to a nitrocellulose membrane. The membrane was blocked with Odyssey blocking buffer (LiCor) for 1 h, followed by incubation with primary antibodies including anti-myc (1:2,000), anti-TDP-43 (1:2,000), anti-α-tubulin (1:10,000) and anti-γ-actin (1:10,000) overnight at 4 °C, and incubation with secondary antibodies (1:10,000, LI-COR) in blocking buffer in PBS with 0.1% Tween 20 for 1 h at RT. Biotinylated proteins were detected with IRDye streptavidin (1:10,000). Blots were scanned on an Odyssey imager (LiCor).

Sample digestion for mass spectrometry analysis. Neutravidin beads were spun down and residual urea was removed. Digestion buffer (200 µL of 50 mM NH₄HCO₃) was added and the bead solution was then treated with 1 mM dithiothreitol (DTT) at 25 °C for 30 min, followed by 5 mM iodoacetimide (IAA) at 25 °C for 30 min in the dark. Proteins were digested with 1 µg of lysyl endopeptidase (Wako) at RT for 2 h and further digested overnight with 1:50 (w/w) trypsin (Promega) at RT. Resulting peptides were desalted with a Sep-Pak C18 column (Waters) and dried under vacuum.

LC-MS/MS analysis. Liquid chromatography coupled to tandem mass spectrometry (LC-MS/MS) on an Orbitrap Fusion mass spectrometer (Thermo Fisher Scientific, San Jose, CA) was performed at the Emory Integrated Proteomics Core (EIPC) essentially as described[57]. The dried samples were resuspended in 10 µL of loading

buffer (0.1% formic acid, 0.03% trifluoroacetic acid, 1% acetonitrile), vortexed for 5 min and centrifuged at maximum speed (20,000g) for 2 min. Peptide mixtures (2 µL) were loaded onto a 25 cm × 75 µm internal diameter fused silica column (New Objective, Woburn, MA) self-packed with 1.9 µm C18 resin (Dr. Maisch, Germany). Separation was carried out over a 120 min gradient by a Dionex Ultimate 3000 RSLCnano at a flow rate of 350 nL/min. The gradient ranged from 3% to 80% buffer B (buffer A: 0.1% formic acid in water, buffer B: 0.1% formic in ACN). The mass spectrometer cycle was programmed to collect at the top speed for 3-s cycles. The MS scans (400–1,600 m/z range, 200,000 AGC, 50 ms maximum ion time) were collected at a resolution of 120,000 at m/z 200 in profile mode and higher-energy collisional dissociation (HCD) MS/MS spectra (0.7 m/z isolation width, 30% collision energy, 10,000 AGC target, 35 ms maximum ion time) were detected in the ion trap. Dynamic exclusion was set to exclude previous sequenced precursor ions for 20 s within a 10-ppm window. Precursor ions with +1 and +8 or higher charge states were excluded from sequencing.

Database search. All raw data files were processed using the Proteome Discoverer 2.0 data analysis suite (Thermo Scientific, San Jose, CA). The database was downloaded from Uniprot (15 April 2015) and consists of 53,291 mouse target sequences supplemented with 2 BirA*-fusion sequences. Peptide matches were restricted to full tryptic cleavage, a precursor mass tolerance of ±10 ppm and a fragment mass tolerance of 0.6 Da. Dynamic modifications were set for methionine oxidation (+15.99492 Da), asparagine and glutamine deamidation (+0.98402 Da), lysine ubiquitination (+114.04293 Da), biotinylation (+226.2994 Da) on the N terminus and lysine and protein N-terminal acetylation (+42.03670). A maximum of three modifications were allowed per peptide (up to two missed cleavages) and a static modification of +57.021465 Da was set for carbamidomethyl cysteine. The Percolator[58] node in Proteome Discoverer was used to filter the peptide spectral match (PSM) false discovery rate to 1%.

Identification of the TDP-43 and TDP-CTF interactome. Urea homogenates were collected from N2a cells transfected with expression vectors for GFP (Mock control), BirA*-TDP-43 and BirA*-TDP-CTF. The experiment was performed with two biological replicates. Four different comparisons of proteomic data were performed: (1) BirA*-TDP-43 versus Mock control; (2) BirA*-TDP-CTF versus Mock control; (3) BirA*-TDP-43 versus BirA*-TDP-CTF; and (4) BirA*-TDP-CTF versus BirA*-TDP-43. To filter the results, in comparisons 1 and 2, a protein was identified as TDP-43 or TDP-CTF associated if there was no missing data, the average number of PSMs in the TDP-43 or TDP-CTF associated proteome was ≥10 and Mock ≤2. In comparisons 3 and 4, the same criteria were also applied to a protein considering a TDP-43-preferred interactor when the PSM in BirA*-TDP-43 was ≥10 and Mock ≤2, and the fold increase was ≥2^{0.5} as compared to the PSM in BirA*-TDP-CTF, and vice versa. Mock control cells provided the background levels of endogenous biotinylation and nonspecific pulldown. The identification of BirA*-TDP-43- or BirA*-TDP-CTF-preferred interactors addresses their cellular compartment- and function-specific roles. These proteins were analyzed and categorized on the basis of biological process, cellular component and molecular function using the Database for Annotation, Visualization, and Integrated Discovery (DAVID) Bioinformatic Resources 6.8 (https://david.ncifcrf.gov/).

Bioinformatics analyses. Prion-like amino acid composition of human Nups and TFs was predicted by the open-source PLAAC algorithm (http://plaac.wi.mit.edu/). The log-likelihood ratio (LLR) score allows the exploratory screening of potential PrLDs. Since low content of hydrophobic residues and high net charge are known predictors for low-complexity sequence domains and intrinsically disordered proteins, we performed a predictive analysis of mean hydrophobicity using ProtScale (https://web.expasy.org/protscale/) with the hydrophobicity scale of Kyte and Doolittle. Hydrophobic amino acids include alanine (1.8), cysteine (2.5), glycine (−0.4), isoleucine (4.5), leucine (3.8), methionine (1.9), phenylalanine (2.8) and valine (4.2), and hydrophilic residues include arginine (−4.5), asparagine (−3.5), aspartate (−3.5), histidine (−3.2), lysine (−3.9), proline (−1.6), glutamine (−3.5), glutamate (−3.5) and tyrosine (−1.3). Low-complexity and intrinsic disorder predictions were performed using DisEMBL version 1.5 (http://dis.embl.de/) and GlobPlot version 2.3 (http://globplot.embl.de/) to validate the relationship between hydrophobicity and protein intrinsic disorder in human Nups and TFs.

Immunofluorescence and image acquisition and analysis. To validate the interaction of Nups and TFs with TDP-CTF, N2a cells were cotransfected with expression plasmids for GFP or epitope-tagged Nups or TFs (Supplementary Table 3) and mCherry or mCherry-tagged TDP-CTF. Cells were fixed with 4% paraformaldehyde (PFA) in PBS 48 h after transfection for 15 min at RT, permeabilized with 0.2% Triton X-100 in PBS for 5 min and blocked with 5% bovine serum albumin (BSA) for 45 min. Cells were incubated with primary antibodies including anti-myc (1:200), anti-Flag (1:500), anti-HA (1:500), anti-T7 (1:500), anti-TDP-43 (1:500), anti-pTDP-43 (Ser409/Ser410) (1:500), anti-SQSTM1/p62 (1:1,000), anti-nuclear pore complex proteins (mAb414; 1:1,000), anti-Nup98 (1:500), anti-Nup205 (1:100), anti-Lamin B (1:200), anti-Sun2 (1:100),

anti-Nesprin-2 (1:100), anti-Ran (1:500), anti-RanGAP1 (1:300) and anti-γH2AX (1:500) overnight at 4 °C, followed by incubation with fluorophore-conjugated secondary antibodies and streptavidin for 1 h at RT. F-actin was labeled with Alexa Fluor 488 or rhodamine-conjugated phalloidin (1:1,000) for 1 h at RT.

To examine DNA damage, cortical neurons were transfected with expression plasmids for GFP or GFP-tagged TDP-CTF, TDP-43^{WT} or TDP-43^{Q331K}. γH2AX has been identified as the marker of DNA double-strand breaks[59]. The mean pixel intensity of stained γH2AX in the nucleus of human fibroblasts and transfected cortical neurons was analyzed by ImageJ software (National Institutes of Health). DNA-damage-inducing calicheamicin γ1 was added at 5 nM for 2 h as a positive control.

To quantitate the percentage of cells that have morphological abnormalities in the NM stained with anti-lamin B or anti-RanGAP1 antibodies, the presence of irregularity, distortion or rifts in the NM was scored. For 3D reconstructions of whole nuclei, lamin B staining was used to outline the nuclear region of cortical neurons. On average 45 to 50 z-stack sections at 0.3 µm steps were required to reconstruct the whole nucleus using Imaris software (Bitplane). A surface was created to mask the nucleus with a smoothing factor of 0.3 µm. Optical sections in the xy, xz and yz planes were generated.

To investigate the nucleocytoplasmic transport of proteins, NES-tdTomato-NLS, a protein transport reporter[60], was transfected into human fibroblasts or cotransfected with expression plasmids for GFP or GFP-tagged TDP-CTF, TDP-43^{WT}, TDP-43^{Q331K}, TDP-43^{M337V} or TDP-43^{mtNLS} into cortical neurons. The mean pixel intensity of NES-tdTomato-NLS and GFP-TDP-43 in the nucleus and cytoplasm were measured for calculating the nuclear-to-cytoplasmic (N-to-C) ratio. To examine whether induction of apoptosis causes a similar defect in the nucleocytoplasmic transport of proteins, the GFP-transfected cells were incubated with staurosporine at 50 nM or 250 nM for 12 h to induce caspase-3/9-dependent apoptosis[61]. The inhibition of nuclear protein import was induced by importazole[62] at 2.5 µM or 5 µM for 12 h. DMSO was added as the vehicle control.

For high-resolution imaging, z-series (15–50 sections, 0.15–0.3 µm steps) were acquired according to the different experimental designs with an epifluorescence microscope (Ti, Nikon) equipped with a cooled CCD camera (HQ2, Photometrics). Within each experiment, all groups were imaged with the same acquisition settings. Image stacks were deconvolved using a 3D blind constrained iterative algorithm (AutoQuant, Media Cybernetics).

For visualization of NPCs, super-resolution 3D structured illumination microscopy (SIM) was performed on a Nikon microscope using a 100× (1.49 NA) objective. Ten to 30 z-stacks were acquired per image to capture the entire nuclear volume and SIM reconstructions were performed in NIS elements (Nikon). Fourier transformations were applied to assess reconstruction quality. 3D SIM images were analyzed in ImageJ. Series of widefield images were acquired and merged with the super-resolution image of Nup98 and mAb414 staining.

For imaging iPSC-derived neurons, images were taken on a LSM800 confocal microscope using Airyscan mode super-resolution. All images represent z optical slices of the nuclear membrane. Eighty to 90 cells were analyzed per group per staining.

Fluorescence in situ hybridization (FISH) and immunofluorescence. Cortical neurons and human fibroblasts were washed with PBS and fixed with 4% PFA in PBS for 10 min. FISH was performed with some modifications of a previously described method[63]. Briefly, fixed cells were permeabilized with 50%, 70% and 100% ethanol in successive steps, stored at −20 °C for overnight and rehydrated the next day with 1× SSC for 10 min. Cells were washed with 10% formamide (Sigma-Aldrich) for 5 min and incubated in hybridization buffer (20% dextran sulfate, 4× SSC, 4 mg/mL BSA, 20 mM ribonucleoside vanadyl complex and 10 mM sodium phosphate buffer, pH 7.0) at 37 °C for 1.5 h. To detect poly(A) RNAs, 1 µL of 25 µM biotinylated oligo(dT) probes (Biosearch Technologies) were resuspended with 10 µg each of E. coli tRNA and salmon sperm DNA in 50 µL of hybridization buffer and incubated on the coverslips at 37 °C overnight. Oligo(dA) probes were used as a negative control. Cells were washed with PBS for 10 min to remove formamide, blocked with 5% BSA for 45 min and incubated with Cy3-conjugated streptavidin for 1 h at RT to detect the biotinylated oligo(dT) probes. Mean pixel intensities for poly(A) RNA in the nucleus and cytoplasm of cells were determined with ImageJ software.

Metabolic labeling of newly synthesized proteins. Cortical neurons were transfected with expression vectors for GFP or GFP-tagged TDP-43^{WT} or TDP-CTF. After 24 h, cells were incubated in methionine-free DMEM (Thermo Fisher Scientific) with or without 40 µM anisomycin (Sigma-Aldrich) for 1 h at 37°, followed by incubation with 100 µg/mL L-azidohomoalanine (AHA) (Thermo Fisher Scientific) for 5 min. Cells were washed with PBS and fixed by 4% PFA, permeabilized with 0.2% Triton X-100 for 5 min and blocked with 3% BSA in PBS for 30 min. Click-iT reaction cocktail (50 µL per sample) was prepared immediately before the end of blocking using Click-iT assay kits and Alexa Fluor 647-conjugated alkyne (Thermo Fisher Scientific). Samples were incubated for 30 min at RT and washed with 3% BSA in PBS before mounting. The mean pixel intensity of AHA in the cell body was quantified with ImageJ software.

Electron microscopy of the nuclear envelope. To visualize nuclear envelope morphology in transfected N2a cells by electron microscopy, we used fusion constructs of the engineered APEX2 peroxidase with Flag-tagged TDP-43 and TDP-CTF[20]. N2a cells were transfected with expression plasmids for Flag-APEX2-TDP-43, Flag-APEX2-TDP-CTF or GFP-TDP-CTF. Cells were fixed with PFA and 2.5% glutaraldehyde in 0.1 M phosphate buffer. APEX2 catalyzes the deposition of 3,3′-diaminobenzoic acid (DAB), which allowed us to identify APEX2-TDP-43- and APEX2-TDP-CTF-expressing cells under electron microscopy (JEOL JEM-1400).

Immunohistochemistry. All procedures for collection of human brain tissue were approved by the Emory University and Mayo Clinic Institutional Review Board. Informed consent was obtained from all patients or their authorized legal representatives. Paraffin-embedded sections from post-mortem human motor and frontal cortex, hippocampus and cerebellum at 8 μm thickness were deparaffinized by incubation in a 60 °C oven for 30 min and rehydrated by immersion in Histo-Clear and 100% ethanol and 95% ethanol solutions. Antigen retrieval was then performed by microwaving sections in 10 mM citrate buffer, pH 6.0, for a total of 5 min and allowing them to cool to RT for 30 min. Peroxidase quenching was performed by incubating sections in a 3% hydrogen peroxide solution in methanol for 5 min at 40 °C and then rinsing in Tris-Brij buffer (1 M Tris-Cl pH 7.5, 100 mM NaCl, 5 mM MgCl$_2$, 0.125% Brij 35). For blocking, sections were incubated in normal goat serum (Elite Vectastain ABC kit) for 15 min at 40 °C. Sections were then incubated with Nup205 (1:50), lamin B1 (1:300) or RanGAP1 (1:50) antibodies (diluted in 1% BSA in Tris-Brij 7.5) overnight at 4 °C. The following day sections were incubated in biotinylated secondary antibody at 5 μL/mL (Elite IgG Vectastain ABC kit) for 30 min at 37 °C and then incubated with the avidin-biotin enzyme complex (Vector Laboratories) for 30 min. Stains were visualized by incubation of DAB chromogen (Sigma-Aldrich) for 5 min at RT. Slides were then dehydrated in an ethanol series and mounted on cover slips. Investigators were blinded for quantitative analysis of IHC staining.

Statistical analysis. Statistical analysis was performed with unpaired *t*-test, one-way ANOVA or two-way ANOVA based on the experimental design. Bonferroni's post hoc test was used. No statistical methods were used to predetermine sample sizes, but our sample sizes are similar to those reported in the previous literatures in the field[33,39,64]. Data distribution was assumed to be normal, but this was not formally tested. Data collection and analysis were not performed blind to the conditions of the experiments, except for quantitative analysis of human fibroblasts and IHC staining. In this study, no animals or samples were assigned to experimental groups, and therefore no randomization was performed. Data from different experiments were analyzed using GraphPad Prism Software. Differences were considered statistically significant for *P* values < 0.05.

Life Sciences Reporting Summary. Further information on experimental design is available in the Life Sciences Reporting Summary.

Data availability. Data available on reasonable request from the authors. Proteomic source data are available from Synapse (http://www.synapse.org) via accession syn11597066. Figure 2 and Supplementary Figs. 2 and 3 are associated with the source data.

References

51. Ayala, Y. M. et al. Structural determinants of the cellular localization and shuttling of TDP-43. *J. Cell Sci.* **121**, 3778–3785 (2008).
52. Estes, P. S. et al. Wild-type and A315T mutant TDP-43 exert differential neurotoxicity in a *Drosophila* model of ALS. *Hum. Mol. Genet.* **20**, 2308–2321 (2011).
53. Joardar, A. et al. PPAR gamma activation is neuroprotective in a *Drosophila* model of ALS based on TDP-43. *Hum. Mol. Genet.* **24**, 1741–1754 (2015).
54. Williams, K. R. et al. hnRNP-Q1 represses nascent axon growth in cortical neurons by inhibiting Gap-43 mRNA translation. *Mol. Biol. Cell* **27**, 518–534 (2016).
55. Fallini, C., Bassell, G. J. & Rossoll, W. High-efficiency transfection of cultured primary motor neurons to study protein localization, trafficking, and function. *Mol. Neurodegener.* **5**, 17 (2010).
56. Donnelly, C. J. et al. RNA toxicity from the ALS/FTD C9ORF72 expansion is mitigated by antisense intervention. *Neuron* **80**, 415–428 (2013).
57. Rha, J. et al. The RNA-binding protein, ZC3H14, is required for proper poly(A) tail length control, expression of synaptic proteins, and brain function in mice. *Hum. Mol. Genet.* **26**, 3663–3681 (2017).
58. Käll, L., Canterbury, J. D., Weston, J., Noble, W. S. & MacCoss, M. J. Semi-supervised learning for peptide identification from shotgun proteomics datasets. *Nat. Methods* **4**, 923–925 (2007).
59. Kuo, L. J. & Yang, L. X. Gamma-H2AX – a novel biomarker for DNA double-strand breaks. *In Vivo* **22**, 305–309 (2008).
60. Hatch, E. M., Fischer, A. H., Deerinck, T. J. & Hetzer, M. W. Catastrophic nuclear envelope collapse in cancer cell micronuclei. *Cell* **154**, 47–60 (2013).
61. Caballero-Benítez, A. & Morán, J. Caspase activation pathways induced by staurosporine and low potassium: role of caspase-2. *J. Neurosci. Res.* **71**, 383–396 (2003).
62. Soderholm, J. F. et al. Importazole, a small molecule inhibitor of the transport receptor importin-β. *ACS Chem. Biol.* **6**, 700–708 (2011).
63. Fallini, C. et al. The survival of motor neuron (SMN) protein interacts with the mRNA-binding protein HuD and regulates localization of poly(A) mRNA in primary motor neuron axons. *J. Neurosci.* **31**, 3914–3925 (2011).
64. Coyne, A. N. et al. Futsch/MAP1B mRNA is a translational target of TDP-43 and is neuroprotective in a *Drosophila* model of amyotrophic lateral sclerosis. *J. Neurosci.* **34**, 15962–15974 (2014).

nature research

Corresponding author(s): Wilfried Rossoll

☐ Initial submission ☐ Revised version ☒ Final submission

Life Sciences Reporting Summary

Nature Research wishes to improve the reproducibility of the work that we publish. This form is intended for publication with all accepted life science papers and provides structure for consistency and transparency in reporting. Every life science submission will use this form; some list items might not apply to an individual manuscript, but all fields must be completed for clarity.

For further information on the points included in this form, see Reporting Life Sciences Research. For further information on Nature Research policies, including our data availability policy, see Authors & Referees and the Editorial Policy Checklist.

▶ Experimental design

1. Sample size

Describe how sample size was determined.

No statistic analysis was used to predetermine sample size. Sample sizes were chosen to be similar or exceed those reported in the previous literatures in the field. Each experiment was repeated 3-6 times, and the statistical analysis demonstrates that our sample sizes revealed significant differences between groups.

2. Data exclusions

Describe any data exclusions.

No data were excluded from the analyses in all the in vitro studies. For in vivo experiments in Drososophila, outliers were identified with GraphPad Prism, using the ROUT method.

3. Replication

Describe whether the experimental findings were reliably reproduced.

The findings in this study were collected from multiple independent experiments, and were reliably reproduced.

4. Randomization

Describe how samples/organisms/participants were allocated into experimental groups.

No randomization was done in this study, since no samples/organisms/participants were allocated into experimental groups.

5. Blinding

Describe whether the investigators were blinded to group allocation during data collection and/or analysis.

Investigators were blinded for quantitative analysis of human fibroblasts and IHC staining. For studies with transfected cell lines, blinding was not possible due to obvious staining patterns observed in microscopy.

Note: all studies involving animals and/or human research participants must disclose whether blinding and randomization were used.

6. Statistical parameters

For all figures and tables that use statistical methods, confirm that the following items are present in relevant figure legends (or in the Methods section if additional space is needed).

n/a	Confirmed	
☐	☒	The <u>exact sample size</u> (*n*) for each experimental group/condition, given as a discrete number and unit of measurement (animals, litters, cultures, etc.)
☐	☒	A description of how samples were collected, noting whether measurements were taken from distinct samples or whether the same sample was measured repeatedly
☐	☒	A statement indicating how many times each experiment was replicated
☐	☒	The statistical test(s) used and whether they are one- or two-sided (note: only common tests should be described solely by name; more complex techniques should be described in the Methods section)
☐	☒	A description of any assumptions or corrections, such as an adjustment for multiple comparisons
☐	☒	The test results (e.g. *P* values) given as exact values whenever possible and with confidence intervals noted
☐	☒	A clear description of statistics including <u>central tendency</u> (e.g. median, mean) and <u>variation</u> (e.g. standard deviation, interquartile range)
☐	☒	Clearly defined error bars

See the web collection on statistics for biologists for further resources and guidance.

▶ Software

Policy information about availability of computer code

7. Software

Describe the software used to analyze the data in this study.	No custom algorithms or software were used. Graphpad Prism 5.0 was used for statistical analysis. Prion-like amino acid composition of human Nups and TFs was predicted by the PLAAC algorithm (http://plaac.wi.mit.edu/). For predictive analysis of mean hydrophobicity, ProtScale was used with the hydrophobicity scale of Kyte and Doolittle (http://web.expasy.org/protscale/). Low-complexity and intrinsic disorder predictions were performed using DisEMBL 1.5 (http://dis.embl.de/) and GlobPlot 2.3 (http://globplot.embl.de/). Proteins were analyzed and categorized on the basis of biological process, cellular component and molecular function using the Database for Annotation, Visualization, and Integrated Discovery 6.8 (DAVID) (https://david.ncifcrf.gov/). For high-resolution imaging, Z-stacks were acquired with NIS elements (Nikon). Image stacks were deconvolved using a 3D blind constrained iterative algorithm (AutoQuant, Media Cybernetics). For super-resolution 3D structured illumination microscopy, SIM reconstructions were performed in NIS elements (Nikon). 3D SIM images were analyzed in ImageJ v1.48 (https://imagej.nih.gov/ij/). Western blots were scanned with Image Studio Lite 4.0 (https://www.licor.com/bio/products/software/image_studio_lite/). Network analysis of the TDP-CTF versus TDP-43 proteome in the nucleocytoplasmic transport pathway were performed with Cytoscape v3.5 (http://www.cytoscape.org/), using the GeneMANIA (http://apps.cytoscape.org/apps/genemania) and ClueGo (http://apps.cytoscape.org/apps/cluego) plugins.

For manuscripts utilizing custom algorithms or software that are central to the paper but not yet described in the published literature, software must be made available to editors and reviewers upon request. We strongly encourage code deposition in a community repository (e.g. GitHub). *Nature Methods* guidance for providing algorithms and software for publication provides further information on this topic.

▶ Materials and reagents

Policy information about availability of materials

8. Materials availability

Indicate whether there are restrictions on availability of unique materials or if these materials are only available for distribution by a for-profit company.	Unique materials are readily available from the authors, standard commercial sources, or repositories (Addgene [www.addgene.org] and Euroscarf [www.euroscarf.de])

9. Antibodies

Describe the antibodies used and how they were validated for use in the system under study (i.e. assay and species).

Validated antibodies were used as also listed in Supplementary Table 3:
+ Mouse monoclonal anti-myc (9E10) (DSHB Hybridoma Product 9E 10)
Validated for IF, IHC-P, IP, and WB (epitope tag).
+ Mouse monoclonal anti-FLAG (M2) Sigma-Aldrich (F1804)
Validated for WB, IP, ICC, IF (epitope tag).
+ Mouse monoclonal anti-HA (HA.11) Covance (MMS-101R)
Validated for WB, IF, IP (epitope tag).
+ Rabbit polyclonal anti-T7 Millipore (AB3790)
Validated for WB, ICC, IP (epitope tag).
+ Rabbit polyclonal anti-TDP-43 Proteintech Group (12892-1-AP)
Validated for IF, IHC, IP, WB (human, mouse, rat, monkey, zebrafish)
+ Rabbit polyclonal anti-phospho-TDP-43 (S409/410) Cosmo Bio (TIP-PTD-P02)
Validated for WB, IHC (human).
Hasegawa M., Arai, T., Nonaka, T., et al., and Akiyama, H. Phosphorylated TDP-43 in Frontotemporal Lobar Degeneration and Amyotrophic Lateral Sclerosis. Ann. Neurol. 2008 Jul;64(1):60-70.
+ Mouse monoclonal anti-α-Tubulin Sigma-Aldrich (T6074)
Validated for ICC, IP, WB (human, mouse, rat).
+ Mouse monoclonal anti-γ-Actin Santa Cruz (sc-65638)
Validated for WB, IP, IF (mouse, rat, human)
+ Mouse monoclonal anti-SQSTM1/p62 Abcam (ab56416)
Validated for IHC-P, WB, ICC/IF (mouse, rat and human)
+ Mouse monoclonal anti-nuclear pore complex proteins (mAb414) BioLegend
Validated for WB, IHC, IF, IP (vertebrates, Xenopus, yeast).
+ Rabbit monoclonal anti-Nup98 (C39A3) Cell Signalling
Validated for WB, IP, IF (human, mouse, rat)
+ Rabbit polyclonal anti-Nup205 Novus Biologicals (NBP1-91247)
Validated for WB, IHC, IHC-P (human, mouse, rat)
Zhang et al., .Nature. 2015 Sep 3;525(7567):56-61. doi: 10.1038/nature14973.
+ Goat polyclonal anti-Lamin B (M-20) Santa Cruz (sc-6217)
Validated for WB, IP, IF, IHC-P (mouse, rat, and human)
+ Rabbit monoclonal anti-Lamin B1 (EPR8985(B)) Abcam (ab133741)
Validated for IP, ICC/IF, WB, IHC-P (mouse, rat, human)
+ Rabbit monoclonal anti-Sun2 (EPR6557) Abcam (ab124916)
Validated for WB, IHC, ICC/IF (mouse, rat, human)
+ Mouse monoclonal anti-Nesprin-2 (K20-478) Millipore (MABC86)
Validated for WB, ICC, IP (human, mouse)
+ Rabbit polyclonal anti-RanGAP1 (H-180) Santa Cruz (sc-25630)
Validated for WB, IP, IF (mouse, rat and human)
+ Mouse monoclonal anti-Ran BD Biosciences (610340)
Validated for IF, IHC, IP, and WB (human, mouse, rat)
+ Mouse monoclonal anti-phospho-Histone H2AX (Ser139)/γH2AX clone JBW301 Millipore (05-636). Validated for ICC, IF, WB (mouse).

WB=western blot, ICC=immunocytochemistry, ICH-P=immunohisotchemistry (paraffin), IP=immunoprecipitation, IF=immunofluorescence

10. Eukaryotic cell lines

a. State the source of each eukaryotic cell line used.

N2a cells were obtained from ATCC (CCL-131).

b. Describe the method of cell line authentication used.

N2a cells were confirmed as murine cells of neuronal origin (proteomics and ICC).

c. Report whether the cell lines were tested for mycoplasma contamination.

All cell lines tested negative for mycoplasma contamination.

d. If any of the cell lines used are listed in the database of commonly misidentified cell lines maintained by ICLAC, provide a scientific rationale for their use.

None of the cell lines used in this study are listed in the ICLAC database.

▸ Animals and human research participants

11. Description of research animals

Provide details on animals and/or animal-derived materials used in the study.

Timed pregnant C57BL/6 mice (Charles River) were sacrificed, and embryos were collected at embryonic day 16.5 (E16.5). Primary neurons were isolated from both male and female embryos and pooled. In experiments with Drosophila, female and male adults and larvae were used.

12. Description of human research participants

Describe the covariate-relevant population characteristics of the human research participants.

The description of human pathology tissue (age, genotype, clinical and pathological diagnosis) are described in Supplementary Table 2 and listed below:

Case ID/Disease diagnosis/Genetic status/Gender/Age at death (years)/Disease duration (years)/pTDP-43 inclusions in motor cortex:
1 Control --- Female 61 N/A No
2 Control --- Male 56 N/A No
3 Control --- Female 91 N/A No
4 Control --- Female 43 N/A No
5 Control --- Male 66 N/A No
6 Control --- Male 61 N/A No
7 Control --- Male 66 N/A No
8 Control --- Female 66 N/A No
9 Control --- Male 66 N/A No
10 Control --- Male 61 N/A No
11 ALS TARDBP Male 67 3 Yes
12 ALS TARDBP Male 87 4 No
13 ALS C9orf72 Male 67 1.5 Yes
14 ALS C9orf72 Female 64 5 Yes
15 ALS C9orf72 Female 57 2.5 Yes
16 ALS C9orf72 Female 57 7 Yes
17 ALS C9orf72 Male 65 2 Yes
18 ALS C9orf72 Male 69 3.5 Yes
19 ALS C9orf72 Female 55 4 Yes
20 ALS SOD1 Female 65 <1 No
21 ALS Sporadic Male 64 8 Yes
22 ALS Sporadic Female 73 3 Yes
23 ALS Sporadic Female 62 2.5 Yes
24 ALS Sporadic Male 48 3 Yes
25 ALS Sporadic Female 49 1.5 Yes
21 ALS Sporadic Male 61 7 Yes
22 ALS Sporadic Female 68.5 5.5 Yes
23 ALS Sporadic Male 70 2.5 Yes
24 ALS Sporadic Male 70 3.5 Yes
25 ALS Sporadic Male 59 1 Yes
26 ALS Sporadic Male 70 4 Yes
27 ALS Sporadic Male 64 7 Yes
28 ALS Sporadic Male 60 2 Yes
29 ALS Sporadic Female 70 4 Yes
30 ALS Sporadic Female 60 5 Yes

TDP-ALS = ALS patients with TARDBP mutation (G298S and A315T)
C9-ALS = ALS patients with C9orf72 mutation
SOD1-ALS = ALS patient with SOD1 mutation (A4V)
sALS = sporadic ALS